

**Understanding cancer and immune cell heterogeneity
using microfluidics, dielectrophoresis, and conventional
methods**

by
Esra Şengül

Submitted to the Graduate School of Natural Science and Engineering
In partial fulfillment of the requirement for the degree of
Master of Science

Sabanci University
June 2021

Understanding cancer and immune cell heterogeneity using
microfluidics, dielectrophoresis, and conventional methods

APPROVED BY:

[Redacted signature line]

[Redacted signature line]

[Redacted signature line]

[Redacted signature line]

DATE OF APPROVAL: 30/06/2021

© Esra Şengül 2021

All Right Reserved

ABSTRACT

Understanding cancer and immune cell heterogeneity using microfluidics, dielectrophoresis, and conventional methods

ESRA ŞENGÜL

Molecular Biology Genetics and Bioengineering, M.Sc. Thesis, June 2021

Thesis Supervisor: Assoc. Prof. Meltem Elitaş

Keywords: Cell heterogeneity, Conventional cell culture, Dielectrophoresis, Glioblastoma, Invasiveness, Macrophage, Microfluidics, Monocyte

Cell heterogeneity is characterized by the genetic variations, environmental differences, and reversible changes in cellular properties. Phenotypic and functional heterogeneity develops in cells within the same population. This heterogeneity is extensively studied and implemented in different fields, namely, molecular biology, genetics, immunology, cancer biology, cell biology, biochemistry, and biophysics. It is experimentally proven that cell heterogeneity inside the tumor enhances the invasive characteristics of the cancer cells. In this study, Glioblastoma cell line U87 and tumor associated macrophages as well as monocytes were investigated using different lab-on-chip devices, and conventional cell culture techniques. It is aimed to understand the heterogeneity of cells within a single population and direct and indirect culture of cancer and immune cells. Heterogeneity is quantified in population level using conventional cell culture techniques, while microfluidic device enabled to receive single cell level data, dielectrophoresis expanded the results by giving dielectric deformation and position of the single cells real time, continuously. Immunostaining experiments further enhanced heterogeneity by determining biomechanical

properties of cells such as size, invasiveness, mesenchymal phenotype, macrophage polarization, immune cell plasticity in dynamic environment, and expression levels of Vimentin, E-Cadherin, CD68, CD80, CD163, CD11a, CD11b, and CD14. Batch culture assays and microfluidic tools together provided better insights about the behavior of cells. Both macrophage and glioma populations were highly heterogenous. Glioma cells exhibited higher migration rate and lower proliferation rate when there was paracrine signaling with macrophages. Existing lab-on-chip techniques must be developed to analyze thousands of cells and patient-specific samples.

ÖZET

Mikroakışkan, dielektroforezis ve geleneksel yöntemler kullanarak kanser-immün hücre heterojenliğini anlamak

ESRA ŞENGÜL

Moleküler Biyoloji Genetik ve Biyomühendislik, YÜKSEK LİSANS TEZİ, Haziran
2021

Tez Danışmanı: Doç. Dr. Meltem Elitas

Anahtar Kelimeler: Hücre heterojenliği, Glioblastoma, Monosit, Makrofaj,
Mikroakışkanlar, Dielektroforez, Geleneksel hücre kültürü, İnvazivite

Hücre heterojenliği, genetik varyasyonlar, çevresel farklılıklar ve hücresel özelliklerde değişiklikler, fenotipik ve fonksiyonel heterojenlik tek bir popülasyonu oluşturan aynı tip hücrelerde gelişir. Bu heterojenlik, moleküler biyoloji, genetik, immünoloji, kanser biyolojisi, hücre biyolojisi, biyokimya ve biyofizik gibi farklı alanlarda kapsamlı bir şekilde incelenmekte ve uygulanmaktadır. Tümördeki hücre heterojenliğinin kanser hücrelerinin istilacı özelliklerini geliştirdiği deneysel olarak kanıtlanmıştır. Bu tezde, Glioblastoma kanser hücre dizisi U87 ve tümörle ilişkili makrofajların yanı sıra monositler, farklı çip üstü laboratuvar cihazları, moleküler biyoloji tahlilleri ve geleneksel hücre kültürü teknikleri kullanılarak araştırılmıştır. Tek bir popülasyon içindeki hücrelerin heterojenliğini ve kanser-bağışıklık hücrelerinin doğrudan ve dolaylı kültürlerindeki heterojenlik değişimini anlamak amaçlanmaktadır. Heterojenlik, geleneksel hücre kültürü teknikleri kullanılarak popülasyon düzeyinde ölçülürken, mikroakışkan cihaz tek hücre düzeyinde veri almayı sağlamıştır. Dielektroforez, sürekli olarak tek hücrelerin dielektrik deformasyonunu ve konumunu gerçek

zamanlı vermiştir. İmmün boyama deneyleri, hücrelerin büyüklük, istilacılık, mezenkimal fenotip, makrofaj polarizasyonu, dinamik ortamda immün hücre plastisitesi belirlemiştir. Hücrelerin Vimentin, E-Cadherin, CD68, CD80, CD163, CD14, CD11a, CD11b belirteçleri ile özellikleri belirlenmiştir. Mikroakışkan cihazda ve hücre kültürü kaplarındaki deneyler glioma ve makrofaj popülasyonlarında yüksek oranda heterojenite olduğunu doğrulamıştır. Glioma hücrelerinin makrofajlardan elde edilen koşullu kültüründe proliferasyon hızı yavaşlamış, göç hızı artmıştır. Binlerce hücreyi analiz etme ve hastaya özel numunelerde analiz gerçekleştirmek için mevcut çip üstü laboratuvar teknikleri geliştirilmelidir.

ACKNOWLEDGEMENTS

I would like to thank my family for their unconditional love and support. Overcoming the academic obstacles during pandemic would not be possible without their support.

I would like to thank Assoc. Prof Meltem Elitaş for offering her endless support, guidance, valuable experiences and being my second family. Also, I would like to thank our present and former lab members Sümeyra Vural, Ünal Akar, Pouya Sharbati, Hande Karamahmutoğlu, Yağmur Yıldızhan, Umut Barış Göğebakan for their support and cooperation; my jury members: Asst. Prof. Stuart James Lucas and Assoc. Prof. Hüseyin Cumhur Tekin for their valuable feedbacks, time and consideration; our collaborators: Rodrigo-Martinez Duarte, Monsur Islam for the equipment, support and guidance.

Last but not least, a special thanks to all my friends and colleagues that are always there for me. Asuman, Sezgin, Ceyhun, Zeynep, Seden, Hale; I will never forget our laugh-filled dinners, long studies, experiments, giggles, discussions, escapes, celebrations. I compiled lots of memories there. Mert, thank you for existing. Buse, Gökçe, Begüm, Rumeysa, Sercan; you are so special for me, and I am very thankful for all your support and love.

I really enjoyed my time as a research assistant as well. I would like to thank the staff of the Faculty of Sciences and Engineering Dean Office, Student Resources and BIO Faculty, I had the privilege and the opportunity to work with them.

I would like to thank our funding resource The Scientific and Technological Research Council of Turkey (TUBITAK) for the support, grant number, 217S616. I would like to thank Sabanci University Faculty of Sciences and Sabanci University Nanotechnology Research and Applications Center (SUNUM) for equipment and support.

This thesis is dedicated to my beloved brother.

TABLE OF CONTENTS

TABLE OF CONTENTS	4
LIST OF FIGURES	6
LIST OF TABLES	7
LIST OF ABBREVIATIONS	10
CHAPTER ONE: INTRODUCTION	8
Motivation	10
Contributions of the Thesis	11
Outline of the Thesis	11
Publications	12
CHAPTER TWO: THEORY AND LITERATURE REVIEW	1
Glioblastoma microenvironment	1
Overview of Glioblastoma heterogeneity	2
Immune cell heterogeneity	4
Mechanical properties of cells	5
Tools to understand heterogeneity.	6
Conventional methods	6
Microfluidics	8
Dielectrophoresis	9
CHAPTER THREE: MATERIALS AND METHODS	12
Cell culture	12
Glioma Cell Culture	12
Monocyte Cell Culture	12
U937-Macrophage Differentiation	12
Conditional Medium Preparation	13
Microfluidic chip experiments	13
Microfluidic chip fabrication	13
Microfluidic chip preparation and cell culture	14
Dielectrophoresis experiments	15
Device fabrication	15
Low Conductive DEP Buffer Preparation	15
Cell preparation	15
Experimental setup	16
Experimental procedure	16
Image acquisition and statistical analysis	16

Conventional cell culture assays	17
Growth curve	17
Wound healing	17
Boyden chamber assay	18
Spheroid formation	19
Immunostaining and live cell staining	20
Live cell staining	20
Immunostaining	20
Imaging	21
Confocal imaging	22
CHAPTER FOUR: CHARACTERIZATION OF HETEROGENEITY USING CONVENTIONAL TECHNIQUES	Error! Bookmark not defined.
Glioma cell proliferation	23
Glioma cell migration	24
Glioma-Macrophage coculture and spheroid formation	25
Immunostaining of Glioma and Macrophages	26
Immunostaining of spheroids	30
Boyden Chamber Assay	36
CHAPTER FIVE: CHARACTERIZATION OF HETEROGENEITY IN MICROFABRICATED TOOLS	38
Comparison of traditional and microfluidic cell culture of glioma	39
Single-cell migration in microfluidic device	40
Glioma deformation	41
Migration velocity	42
Dielectrophoretic deformation and dielectric responses of Monocyte and Macrophages	45
CHAPTER SIX: DISCUSSION	52
Characterization of Heterogeneity in Microfabricated Tools	52
CHAPTER SEVEN: CONCLUSIONS	58
Conclusion	58
Future research directions	59
BIBLIOGRAPHY	60

LIST OF FIGURES

Figure 2.1: Tumor Microenvironment of GBM.

Figure 2.2: Cells undergoing Epithelial Mesenchymal Transition (EMT).

Figure 2.3: Role of TAMs in cancer.

Figure 2.4.2: Electromechanical changes of cells in dielectrophoresis array.

Figure 3.2.1: Microfluidic chip platform for mechanical phenotyping of Glioblastoma at the single-cell level.

Figure 3.4.3: Cell groups distribution and maintenance conditions in chambers.

Figure 4.1: Glioma cell proliferation in different maintenance conditions.

Figure 4.2: Analysis of U87 and U87-C cells migration by the in vitro wound-healing assay.

Figure 4.3: Spheroid formation

Figure 4.4.1: Comparisons of E-cadherin expressions.

Figure 4.4.2: Comparisons of Vimentin expressions.

Figure 4.4.3: Comparisons of CD68 and CD168 expressions.

Figure 4.4.4: Immunofluorescence staining of CD11a, CD11b, and CD14 in macrophages

Figure 4.5.1: Comparisons of CD80 and E-Cadherin expressions.

Figure 4.5.2: Quantitative comparisons of CD80 and E-cadherin expressions.

Figure 4.5.3: Comparisons of CD163 and Vimentin expressions.

Figure 4.5.4: Quantitative comparisons of CD163 and Vimentin expressions.

Figure 4.5.5: Comparisons of CD68 localizations in glioma and coculture.

Figure 4.6: Comparisons of cell migration in Boyden chambers.

Figure 5.1: Comparison of traditional and microfluidic cell culture of glioma

Figure 5.2: Migration of single cells in the microfluidic cell culture chamber.

Figure 5.3: Deformation indexes of the cells in the microfluidic device.

Figure 5.4.1: Velocity changes for the single glioma cells.

Figure 5.4.2: The velocity of glioma cells in the microfluidic cell culture chamber.

Figure 5.4.3: The average velocity of glioma population under different maintenance conditions.

Figure 5.5.1: Dielectrophoretic responses of monocytes and macrophages

Figure 5.5.2: Comparison between the DEP movement of monocyte and macrophage cells.

Figure 5.5.3: DEP deformation trends of three single monocytes.

Figure 5.5.4: Dielectrophoretic deformation indexes (DDI) of U937 monocytes and U937-differentiated macrophages.

Figure 5.5.6: Comparison of the dielectrophoretic deformation indexes for the monocytes and macrophages without outliers.

Table 2.4.1: Comparison of heterogeneity quantification methods.

Table 3.4.4: Spheroid culture properties in 6-well plate.

Table 3.5.2: Antibody and their targets in immunostaining experiments.

LIST OF ABBREVIATIONS

AFM: Atomic Force Microscopy
ATCC: American Type Culture Collection
AU: Arbitrary Unit
BSA: Bovine Serum Albumin
Cr-blank: Chromium deposited photomask
CF: Crossover frequency
CM: Clausius Mossotti
CMFDA: 5-chloromethylfluorescein diacetate
DDI: Dielectrophoretic Deformation Indexes
DEP: Dielectrophoresis
DI: Deionized
DMEM: Dulbecco's Modified Eagle Media
DMSO: Dimethyl Sulfoxide
E: Electric field
ECM: Extracellular Matrix
EMT: Epithelial Mesenchymal Transition
FBS: Fetal Bovine Serum
GBM: Glioblastoma Multiforme
GSC: Glioma Stem Cell
H: Height
nDEP: Negative Dielectrophoresis
PBS: Phosphate Buffered Saline
pDEP: Positive Dielectrophoresis
PDMS: Polydimethylsiloxane
PFA: Paraformaldehyde
PMA: Phorbol 12-myristate 13-acetate
PSA: Pressure Sensitive Adhesive
RPMI: Roswell Park Memorial Institute
TAM: Tumor Associated Macrophage

TF: Transcription Factor

TPSC: Tissue Culture-treated Polystyrene

W: Width

V_{pp}: Volt peak to peak

1 CHAPTER ONE: INTRODUCTION

1.1 Motivation

Tumor microenvironment has a highly complex organization with highly heterogeneous cancer cells surrounded by various types of immune cells. Characterization of cell heterogeneity in cancer and immune cells is essential for cancer drug development, improving personalized medicine and developing diagnosis techniques. Improvement of conventional techniques to understand heterogeneity can provide important information of cell subpopulations and can enhance development of precise treatment and diagnosis strategies. There are different methods available to quantify heterogeneity such as flow cytometry [1] [2], atomic force microscopy [3], optical stretcher [4] and optical tweezers [5], etc. Although these techniques are well established and specific, they are insufficient as being time-consuming, semi-quantitative and require cell labeling.

Microfabricated tools eliminate the drawbacks of existing techniques and characterize cells without altering their genetics and morphological characteristics [6]. Dielectrophoresis (DEP) does not alter genetics or morphological characteristics of cells and it is a great alternative to the available techniques to evaluate single-cell biomechanical properties. DEP is a quantitative and high-throughput method that enables characterization of cells in a short time with low-cost [6].

Recent studies mostly rely on investigating the changes in dielectrophoretic properties by measuring crossover frequencies and migration differences of cells [7–9]. However, dielectrophoresis induced mechanical deformation is another aspect to define biophysical properties of cells and presents a useful tool for quantification of heterogeneity. Alternatively, microfluidic lab-on-chip devices allow improved dynamic control of environmental variables for high-throughput analysis at the single cell level for longer periods compared with DEP. Microfluidic devices with controlled pressure gradients and well-defined geometric shapes offer extensive throughput of *in-vitro* cell characteristics in terms of shape changes of cells, mobility, and deformability. Understanding immune and cancer cell heterogeneity will strengthen our knowledge to understand infiltration of immune

cells within tumor microenvironment and can be a link between translational and conventional studies [10,11].

Microfabricated tools can give the required physicochemical intricacy to be utilized as models for disease screening while being easy to utilize and modest to create. The consistent development of these tools will unequivocally open another road in the improvement of customized tumor models [12]. It is very important to connect conventional assays to the lab-on-chip techniques, which mostly lack standardization.

1.2 Contributions of the Thesis

This study aims to understand the heterogeneity of cell lines that presents in Glioblastoma tumor microenvironment. In the first part of research, DEP responses and dielectrophoretic deformation indexes of U937 and U937-differentiated macrophages, were investigated. Heterogeneity among these two immune cell types is revealed in terms of dielectrophoretic deformations.

In the second part of the study, U87 cells heterogeneity was revealed at single cell level using a microfluidic platform.

Lastly, coculture of U87 glioma cells and U937-derived macrophages performed in order to measure expressions of Vimentin and E-cadherin proteins, which play an active role in the spread and invasion of glioma cells, and CD68, CD80, CD163, CD11a, CD11b proteins that play an active role in determining whether macrophage cells are M1 or M2.

This study strongly suggests that microfabricated tools are important single cell analysis techniques that mostly compensate the limitations of the existing conventional techniques.

1.3 Outline of the Thesis

Chapter 2 explains the heterogeneity of glioma and immune cell populations in the glioblastoma microenvironment. Cancer cell-immune cell interactions and their heterogeneity is depicted. Dielectrophoresis and microfluidic cell culture chambers were used to perform single-cell level heterogeneity analysis.

Chapter 3 introduces the methods that were used in this study; cell culture, microfluidic chip fabrication and cell culture in chips, 3D Carbon-electrode DEP device, cell preparation,

experimental setup, and procedure. To link the results obtained from microfabricated tools with conventional studies; conventional cell culture assays such as growth curve, wound healing, Boyden chamber assay, nucleus analysis, spheroid formation are explained in Chapter 4. To further investigate mechanical changes, immunostaining of cells and spheroids are explained.

Chapter 5 presents the results of understanding Glioblastoma tumor heterogeneity using microfabricated tools. Mechanophenotyping of Glioblastoma cell line U87 in microfluidic platform is presented. Also, surrounding immune cells: U937 monocytes and U937-differentiated macrophages, deformation, and single cell dielectrophoretic mobilities are presented.

Chapter 6 discusses the results; Chapter 7 concludes the thesis and explains future applications of the study.

1.4 Publications

- M. Elitas, E. Sengul, Quantifying Heterogeneity According to Deformation of the U937 Monocytes and U937-Differentiated Macrophages Using 3D Carbon Dielectrophoresis in Microfluidics, *Micromachines*. 11 (2020) 576. <https://doi.org/10.3390/mi11060576>.
- E. Sengul, M. Elitas, Single-Cell Mechanophenotyping in Microfluidics to Evaluate Behavior of U87 Glioma Cells, *Micromachines*. 11 (2020) 845. <https://doi.org/10.3390/mi11090845>.
- E. Sengul, & M. Elitas, Long-Term Migratory Velocity Measurements of Single Glioma Cells using Microfluidics. *The Analyst*. (2020) <https://doi.org/10.1039/d1an00817j>
- E. Sengul, M. Elitas, Understanding the Role of Macrophages in Brain-Tumor Microenvironment, Journal paper (manuscript in preparation).
- E. Sengul, P. Sharbati, I. Monsur, M. Elitas, Dielectrophoretic characterization and separation of U87-MG glioma cells (manuscript in preparation)
- E. Sengul, O. Kara, Y. Yildizhan, R. Martinez-Duarte, M. Elitas, Single Cell Level Dielectrophoretic Responses Dielectrophoretic Deformations of Monocytes to Quantify Population Heterogeneity, in: *Proc. Annu. Int. Conf. IEEE Eng. Med. Biol. Soc. EMBS, Institute of Electrical and Electronics Engineers Inc.*, 2020: pp. 2221–2226. <https://doi.org/10.1109/EMBC44109.2020.9176521>.
- E. Sengul, M. Elitas, Optimization of U-Net: Convolutional Networks for U-87 human primary glioblastoma cell line segmentation, *Emerging Topics in Artificial Intelligence (ETAI) 2021, SPIE Nanoscience + Engineering*

2 CHAPTER TWO: THEORY and LITERATURE REVIEW

2.1 Glioblastoma microenvironment

Glioblastoma multiforme (GBM) is the most malignant glial type of tumor located in the supratentorial region of the brain, which may be multifocal or multicentric with showing low differentiation, vascular proliferation and necrosis [12], Fig. 2.1. It accounts for half of all primary brain tumor deaths, with patients having an average survival rate of around 14 months [13].

One of the reasons that GBM becomes a deadly and aggressive tumor type is its heterogeneity as the name suggests “Multiforme”. Intratumor heterogeneity of GBM is evident [14–16]. In this heterogeneity, GBM is not only composed of diverse stromal cells, including vascular cells, the various infiltrating and resident immune cells, and other non-neoplastic glial cell types. Brain-resident microglia, infiltrating monocytes/macrophages, reactive astrocytes, endothelial cells, pericytes, neural cells, progenitor stem cells and other immune cell infiltrates are shown in GBM histopathological analysis [17,18]. Some cells have the property of increased tumorigenicity, infiltration, metastasis activity, self-renewing capacity and some have stemness capacity, however, tumor site does not only compose of cancer cells but also contains tumor-infiltrating peripheral immune cells (Fig. 2.2). Such heterogeneity in GBM results in functionally different responses and diminished sensitivity to targeted therapeutics [16].

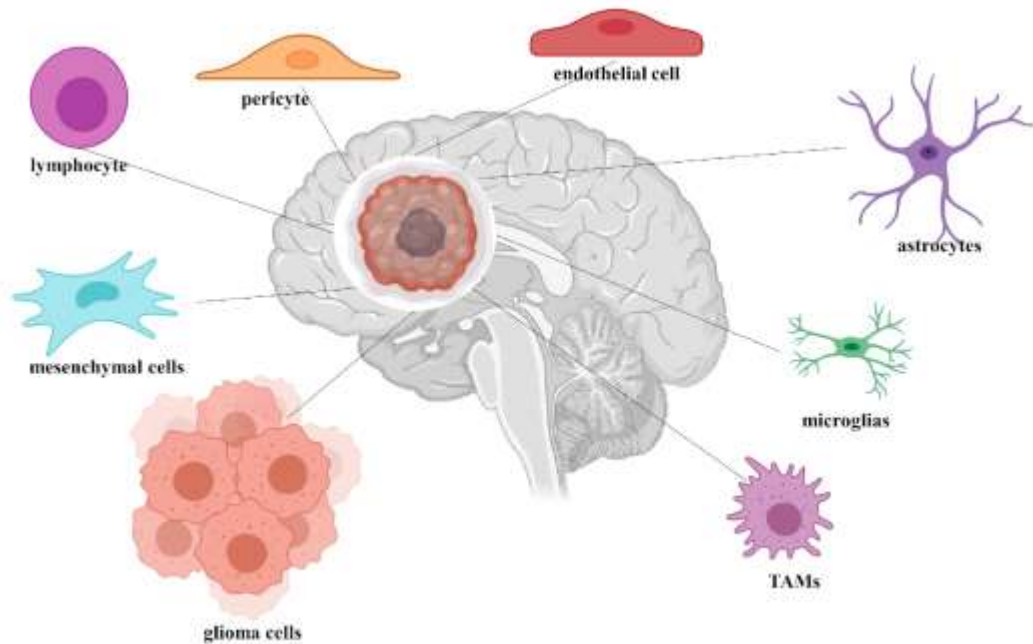


Figure 2.1: Tumor Microenvironment of GBM. On the side of the immune system, tumor-associated macrophages (TAMs), mainly comprised of microglia and peripheral monocytes, are attracted by tumor cells, which release pro-inflammatory cytokines (IL-1 β , IL-6, IL-8, etc.), matrix remodelers and growth factors (TGF β , EGF β , TGF- α , FGFs, PDGF, VEGF, etc.) to aid tumorigenesis [19].

GBM and glioma stem cells (GSCs) are embedded in a heterogeneous tumor microenvironment but also compartmentalized in anatomically distinct regions, coined tumor niches as hypoxic, angiogenic and invasive. These tumor parts can be composed of given cell types and are distinct from each other (Fig.2.1). Vasculature can remain in the center of the tumor and regulate metabolism, immune surveillance, survival, invasion, as well as glioma stem cell maintenance. In the hypoxic part of the tumor, there is either nonviable or receded structure that leads to necrotic areas surrounded by a row of hypoxic palisading tumor cells [20].

2.2 Overview of Glioblastoma heterogeneity

Tumor heterogeneity pertains to existing cell subpopulations within the tissue. Those subpopulations can be distinguished based on genotypic and phenotypic divergence [21].

GBM tumors show significant mitosis and intense infiltration of the surrounding tissues compared with other brain tumors [22]. There are limitations with conventional assays to study such tumors. To the date, mouse models provide the most realistic testing ground, but they still fail to account for the full complexity of tumor-microenvironment interactions, as well as the role of the immune system [23,24].

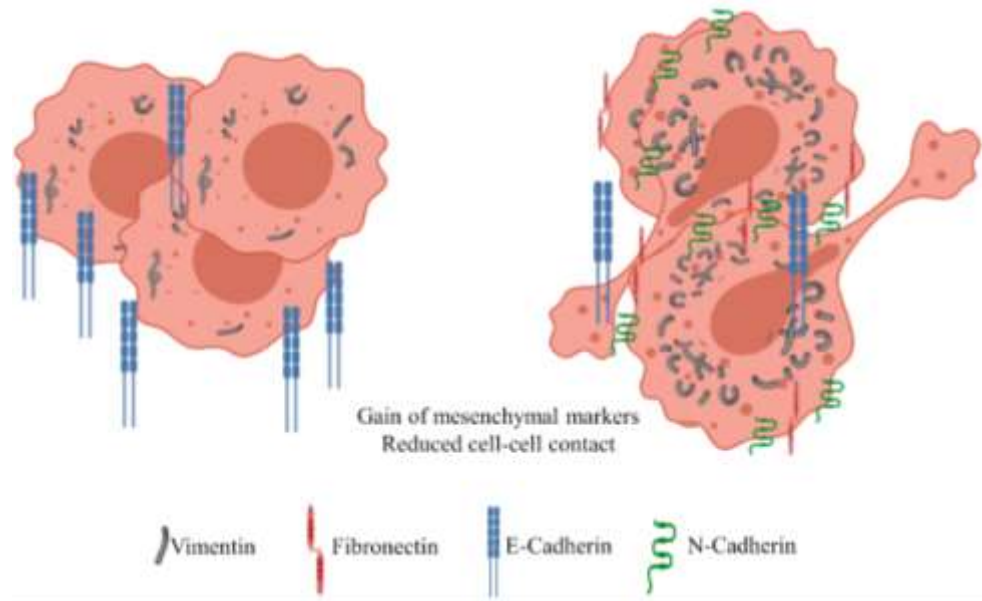


Figure 2.2 Cells undergoing Epithelial Mesenchymal Transition (EMT).

GBM cells are more invasive and resistant to therapy as the epithelial mesenchymal transition (EMT) is highly activated [25,26]. Activation of EMT is crucial for processes involving stem cell formation, wound healing and carcinoma progression since cells gain motility and invasiveness [27]. The environmental changes may enable GBM-like high invasive cancer cells to become more resistant to therapies as they are able to induce EMT [28,29].

Normally cancer cells have strong tight, gap and adherens junctions and they are bound by a basal lamina to the surface, Figure 2.2. Mesenchymal cells have spindle-shape morphology, and they are loss of strong adherens junctions and tend to interact through focal points [30]. Lower expression of E-cadherin is deemed to be an essential for EMT. Besides, Snail 1, Snail 2, ZEB1, ZEB2, TCF3 and KLF8 like transcription factors (TFs) can bind to the E-cadherin promoter and repress it [31,32]. Expression level of E-Cadherin decreases in EMT whereas N-cadherin, fibronectin and vimentin expression levels increase in cells

conducting EMT. (Fig.2.2). Therefore, EMT causes several phenotypic and morphological changes that may affect cytoskeletal, mechanical changes within the cell [33].

2.3 Immune cell heterogeneity

Monocytes and macrophages can be considered as active machines that can immediately adapt to their microenvironment for pathogenesis and homeostasis through altering their either phenotypic or genetic properties [20,34]. They are highly heterogeneous cells as it pertains to their morphology, location, tissue-specific relations, and functional capabilities [35,36]. Macrophages are subtyped into M1 as classically activated macrophages and the M2 as alternatively activated macrophages [37]. It's become clear that alternatively activated macrophages are biochemically and functionally distinct from regulatory macrophages [38].

M1 macrophages are activated by LPS and IFN-gamma and secrete high levels of IL-12 and low levels of IL-10. While the M1 macrophages mostly function in antibacterial and phagocytic events, the M2 macrophages function in wound healing and tissue homeostasis and secretion of IL-10 [39]. The M1 subtype suppresses while the M2 subtype promotes tumor growth.

Tumor-associated macrophages mainly arise from M2 phenotype [40] [41] and are one of the key players in tumor development and progression in many types of cancer [42]. TAMs are monocyte-derived immune cells and are classified based on their cytokines and immune functions as M1- and M2-polarized subtypes [43]

TAMs interact with tumor cells, produce cytokines, stimulate tumor growth, metastasis, invasiveness, and angiogenesis, and inhibit T cell immune response [44]. TAMs are activated by tumors and stimulate tumor cells during carcinogenesis. TAMs, as differentiated immune cells in tumors, arrange several factors in the tumor microenvironment [45]. They play an important role in connecting inflammation with cancer (Fig. 2.3) by promoting proliferation, invasion, and metastasis of tumor cells, stimulating tumor angiogenesis, and inhibiting antitumor immune response mediated by T cells. The tumor-promoting role of macrophages in inflammation is supported by several lines of evidence, including genetic analysis [46,47]. Inflammatory reactions and infiltrated macrophages can promote tumor progression.

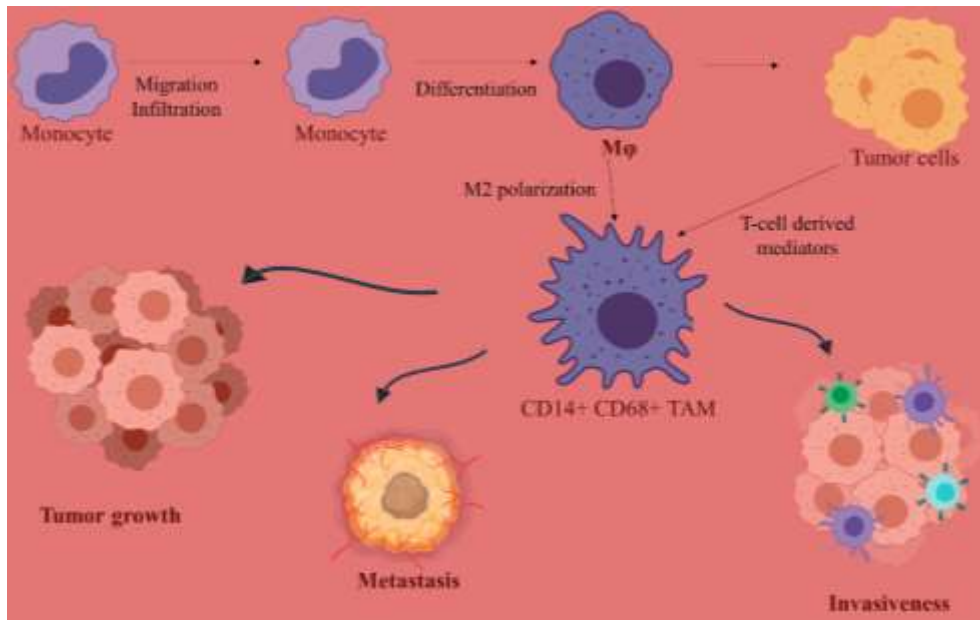


Figure 2.3: Polarization and role of TAMs in the tumor microenvironment (This figure adapted from [44]).

When examined by electron microscopy, the monocytes are spherical cells, they have microvilli and microcytic vesicles, hence their membrane surfaces have several ruffles and blebs. Whereas macrophages have an irregular shape with electron-dense membrane-bound lysosomes. Besides, the microenvironment in which macrophages differentiate defines their shape, biochemistry and function [48]. In general, the monocytes and macrophages enroll in tumor formation and invasion via metastasis and angiogenesis [49,50], pathogen recognition, phagocytosis [51], removal of dead cells and cellular debris [52] and tissue homeostasis [49,53]. Their diverse functions are continuously controlled by their microenvironment [54–57].

2.4 Mechanical properties of cells

Mechanical properties of cells are closely linked to the healthy condition of the cell and have been an important marker for cell state. They are an indicator of nuclear changes, various disease processes and changes in cell status associated with deformation of the cytoskeleton [58]. To date, cell shape has been considered as a key factor for growth control, Folkman and Moscona showed tissue culture plastic adhesivity varies by different concentrations of substrates and they concluded the growth is directly related to cell shape

[59]. Besides, dynamic changes in cell shape may address malignancy with cytoskeletal changes. Fluid and solid physics principles enable us to associate these mechanical cell property changes with biological systems, astonishingly with a low number of cells [60].

2.5 Tools to understand heterogeneity.

2.5.1 Conventional methods

Conventional methods to assess cell heterogeneity includes high throughput screening, cancer research, drug discovery and development, environmental monitoring, biosensing, and gene expression studies, etc. [61–63]. They are now facilitated by both a renewed understanding of cellular heterogeneity and recently developed technologies [64]. Conventional methods may include flow cytometry [1,2], atomic force microscopy [3], optical stretcher [4] and optical tweezers [5], micropipette aspiration [65], parallel-plate rheology [66], microfluidic ektacytometry[67], etc., *Table 2.5.1*

Flow cytometry has been widely used as a fluorescence labelling technique which enables single cell deformation analysis and cell sorting from heterogeneous mixture, however, it requires careful assistance for sticky cells, and usually, density-based outputs received [68,69]. Atomic force microscopy (AFM) is used to measure mechanical dynamics in the instantaneous cellular Young's (extensional) modulus and viscous deformation. AFM may have some limitations in terms of requiring fluorescent fusion proteins or magnetic beads [70]. Optical forces are commonly used in single cell analysis; optical tweezers can be used in cell manipulation with gradient/ scattering forces and optical stretchers are used to detect single cells in the same concept coupled with several other functionalities, such as accurate cellular sorting, trapping, and multiple parallel analysis of cell mechanics [71]. Micropipette aspiration is used to measure mechanical properties according to the length of aspiration, but it is unable to give results at single cell level within the population [72]. Parallel plates rheometer extracts the Young's modulus and deformability similarly to AFM and a single cell placed between a rigid plate and a flexible plate and deformability are measured under exposure to external stresses [66,73]. Microfluidic ektacytometers measure shape changes of particles in viscous media by enabling to analyze the only shear-induced deformability changes [67,74].

It has been difficult to define the mechanical properties of cells in terms of deformability and mechanical plasticity with conventional cell culture techniques as they are time consuming and additional assays are usually required for cell preparation. The bulk blended responses of a population include a high number of cells which may cause misleading analysis results caused by bimodal distribution of cell properties and population heterogeneity [75].

Table 2.5.1: Comparison of heterogeneity quantification methods.

Methods/ Tools	Main beneficial features	Shortcuts	Sample recover y	Label free	High throughp ut	Re f.
DEP (Dielectrophoresis)	Ability to classify each cell depending on its size, shape and electrical properties. It enables them to perform manipulation and receive accurate responses in a short time.	It requires optimized low conductive buffers to keep cells remain viable.	Hig h	Yes	Yes	[7 6]
Flow cytometer/ FACS	Ability of sorting a heterogeneous cell mixture depending on their size and fluorescent characteristics.	The output is density of population, not single-cell level. Dead and sticky cells need more assistance.	Hig h	No	Yes	[6 9]
AFM (Atomic Force Microscopy)	It gives information of sample surface at high resolution level.	It's an expensive and time-consuming method which requires specialized nanostructures as support surfaces.	No	Yes	Yes	[7 7]
Optical Tweezers	Ability to trap and manipulate cells using laser at single-cell level.	It's labor-intensive method, photodamage and sample-heating limits the usage.	No	Yes	No	[7 8]
Micropip ette aspiration	The length of aspiration can be used to measure mechanical properties.	It's unable to measure single cell deformability within the population.	Hig h	Yes	No	[7 9]
Microflui dic	It measures shape change in viscous media	Ability to measure only	Poo r	Yes	No	[7 4,80]

ektacytometry		shear-induced deformability				
Microfluidic constriction channels	It can detect small deformability changes using homogenous flow and viscoelastic properties of cells.	It requires specifically designed channels for each cell type and high-speed microscopy and image analyzing software.	Por	Yes	Yes	[81,82]

The changes in GBM cells occur fast and kinetic responses cannot be easily determined in conventional methods due to required high numbers of cells, cell preparation steps, additional instrument needs, etc. Thus, new techniques to investigate single cell properties are needed instead of bulk techniques.

2.5.2 Microfluidics

Single cell approaches are required to distinguish rare subclones [83]. Microfluidic lab-on-chip devices allow improved dynamic control of environmental variables for high-throughput analysis at the single cell level. Microfluidic devices with controlled pressure gradients and well-defined geometric shapes offer extensive throughput of *in vitro* cell characteristics in terms of shape changes, mobility, deformability and single cell analysis. In such systems, the cell microenvironment and physical interactions are well controlled and continuous aspiration of fresh culture medium, manipulation of cells by changing biophysical and biochemical parameters and real-time imaging and monitoring of the cell culture are enabled [84]. Micrometer-sized microchannels are important to achieve an *in vivo*-like environment for cells. Microfluidics can be scaled by a high surface area to volume ratio compared to standard cell culture systems [85,86]. Microfluidics aims to mimic *in vivo* cellular environment by enabling microliter medium volumes, very low medium-to cell volume ratios and efficient oxygen supply [87]. A particular focus in microfluidics explores the connections among cell structures, biophysical changes and the environmental relationships. It answers how these structural changes alter single cell mechanical responses [88]. According to the study done with a microfluidic optical stretcher by Guck et al., cancerous breast carcinoma cells (MCF7) have slightly more deformation compared to breast

epithelial cells (MCF10A) [60]. Microfluidic channels may offer more quantitative results for cell deformability and motility compared to other methods [88].

To date, numerous cell line models of GBM have been established and used in enormous numbers of studies over the years. These cell lines are the basis of biological research, yet the experiments are usually performed in 2-dimensional (2D) culture systems. Administration of microfluidic culture systems with specialized conditions provide a route to overcome problems of conventional systems and be a better model to mimic cancer microenvironment.

2.5.3 Dielectrophoresis

Dielectrophoresis (DEP) has been used in several cell characterization studies by determining electrical properties of mammalian cells such as measuring electrokinetic properties during growth [89], electrophoretic mobilities of immune cell subpopulations [90], electrophoretic mobility changes of differentiated white blood cells [91]. DEP stands out as a possible alternative to AFM, confocal microscopy and optical rheology to investigate cell heterogeneity. DEP is a method in which dielectric force is applied to the particle when exposed to a non-uniform electric field [49]. Using electrical forces to study cell heterogeneity allows direct characterization of cells based on their intrinsic properties without altering their genotype and phenotype.

DEP offers the possibility to affect the movement of polarized particles in the non-uniform electric field. We can define the DEP force according to the difference between the dielectric properties of the particle and its suspension medium [92].

$$F_{DEP} = 2\pi r^3 \varepsilon_m \text{Re}(K(\omega)) \nabla E^2 \quad (1)$$

The DEP force (F_{DEP}) is related to the radius of the particle, the permittivity of the surrounding medium (ε_m), the real part of the Clausius-Mossotti factor ($\text{Re}(K(\omega))$) and the applied electric field (E).

The radius shows that the phenotypic characteristics of the cells are strictly linked to the health status of the cell and can consequently influence the DEP force or the permittivity. The DEP force is highly related to a larger cell radius with the membrane and the cell interior. When using a single-shell model, these differences would affect the force in the same field and may change cell dielectric parameters [93,94]. The movement of the particle in the

microchannel is provided by the induced dipole moment. The dipole moment (m) varying under the electric field (E), its size and charge depend on the polarity property of the particle per unit volume. The unitless term determined by the polarity rates between the particle and the liquid expressed by the Clausius Mossotti (CM) factor gives an idea about the direction and magnitude of the dipole moment. The Clausius-Mossotti factor is defined as given by

$$K(\omega) = \frac{(\varepsilon_c^* - \varepsilon_m^*)}{(\varepsilon_c^* + 2\varepsilon_m^*)} \quad (2)$$

Here, ε_c^* is known as the complex permittivity of a cell and ε_m^* is the complex permittivity of the surrounding medium. The subscripts “m” and “c” mean suspending medium and cells, respectively. The complex permittivity can be expressed as

$$\varepsilon^* = \varepsilon + \frac{j\sigma}{\omega} \quad (3)$$

where ε is the permittivity, σ is the conductivity and ω ($\omega = 2\pi f$) includes the electric field frequency. If the particle can be more polarized than the suspension medium, more charge is collected on the particle surface, or vice versa. When the value of the $Re(K(\omega))$ is positive, the particle is attracted by the strong electric field region referred to as positive DEP (pDEP). When the value of the $Re(K(\omega))$ is negative, the particle is repelled by the high electric field region referred to as negative DEP (nDEP). The crossover frequency can be defined as the cessation of the particle motion, which is specific for the particles. Hence, crossover frequency can be used to characterize the dielectric properties of cells.

DEP can be used as a quantitative tool to analyze biophysical properties of cells, especially in the concept of kinetic mobility, dielectric mobility and dielectric deformation (Fig. 2.4.2.).

DEP has many advantages, such as cells remain viable, maintain their genetic and phenotypic properties [92] and it is a low-cost technique in terms of not requiring fluorescent labels on the cells [96,97]. Dielectrophoretic responses of cells can be monitored when the cells are exposed to the nonuniformly distributed electric field in the low-conductive suspension medium [6].

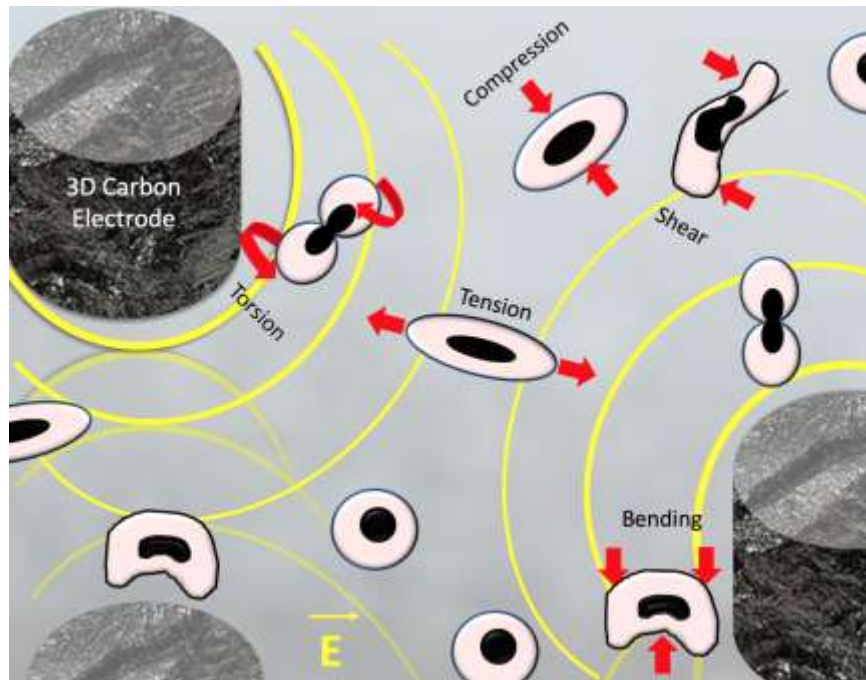


Figure 2.5.3: Electromechanical changes of cells in dielectrophoresis array [98].

3 CHAPTER THREE: MATERIALS and METHODS

3.1 Cell culture

3.1.1 Glioma Cell Culture

The U87-MG (HTB-14™) human glioma cell line obtained from ATCC® (Cat. No. HTB-14™) were cultured in Dulbecco's Modified Eagle Media (DMEM, Pantech), 10% Fetal Bovine Serum (FBS), 1% Pen/Strep (Thermo Fisher Scientific Inc., Waltham, MA, USA) in a standard humidified incubator (NUVE, Turkey) with an atmosphere containing 5% CO₂ at 37°C. The second condition is prepared by U87 cells which were cultured in Roswell Park Memorial Institute Medium 1640 (RPMI 1640) medium used by macrophages for 48 h. In this condition's media U87 cells are maintained with 50% macrophage used RPMI and 50% DMEM. These conditions were used for all experiments unless stated below.

3.1.2 Monocyte Cell Culture

The U937 (CRL-1593.2™) human histiocytic lymphoma monocyte cell line was purchased from ATCC . The U937 monocytes were maintained in RPMI 1640 medium (Roswell Park Memorial Institute, Pan Biotech, Germany), 10% FBS (Sigma Aldrich, St. Louis, MO).

3.1.3 U937-Macrophage Differentiation

The human histiocytic lymphoma macrophages were differentiated from the U937 monocytes through stimulation of 3×10^5 cells/ml in 5 ml RPMI 1640, 10% FBS with 5 µl working solution of 10% Phorbol 12-myristate 13-acetate (PMA, Pan Biotech, Germany) obtained from 10 ng/ml PMA/ dimethyl sulfoxide (DMSO, Pan Biotech, Germany) stock solution according to standard protocols for macrophage differentiation.

3.1.4 *Conditioned Medium Preparation*

Conditioned medium was harvested from U937-differentiated macrophages grown in RPMI 1640, 10% FBS for 72 hours at 37°C with 5% CO₂. The collected media was centrifuged at 3000 rpm for 5 minutes (Z601039 - Hettich® EBA 20 centrifuge, MERCK, Darmstadt, Germany) and filtered through a 0.2- μ m filter (GVS Filter Technology, United Kingdom), the harvest is freshly used in the experiments.

3.2 **Microfluidic chip experiments**

3.2.1 *Microfluidic chip fabrication*

Microfluidic chips were designed using the CleWin 4.0 layout editor. The microfluidic cell culture platform has one inlet and one outlet for medium feeding, and cell loading. The microchamber allows cells to be cultured and visualized (1280 μ m x 500 μ m, h = 50 μ m) with two types of pillars. The circular pillars (r = 90 μ m, h = 50 μ m) avoid polydimethylsiloxane (PDMS) collapse, while the trapezoid pillars connect the medium channel (100 μ m x 50 μ m) to the cell culture microchamber. The distance between the pillars is 390 and 190 μ m for the circular and trapezoidal ones, respectively. The designs were patterned on thin-film chromium deposited photomask (Cr-blank) using a Vistec/EBPG5000plusES Electron Beam Lithography System. SU-8 2025 (SU-8® 2025, MicroChem) was spin-coated on a 4 inches silicon wafer to obtain structures of height 50 μ m. Next, the photoresist-coated wafers were soft baked (65°C, 3 min and 95°C, 5 min) and exposed to UV light (160 mJ/cm⁻², Midas/MDA-60MS mask aligner). Upon two consecutive post-baking processes (65°C, 1 min and 95°C, 5 min), the SU-8 was developed (MicroChem's SU-8 developer). The microfluidic chips were obtained using elastomeric polymer PDMS (Sylgard® 184, Dow Corning, Midland, MI, USA) [80]. 5-mm biopsy punchers (Robbins Instruments, Chatham, MA, USA) were used for the inlet and outlet ports (Fig.3.2.1.a). The PDMS chips were irreversibly bonded on glass slides (Fig.3.2.1.b) using the Corona system (BD20-AC, Electro-Technic Products Inc.).

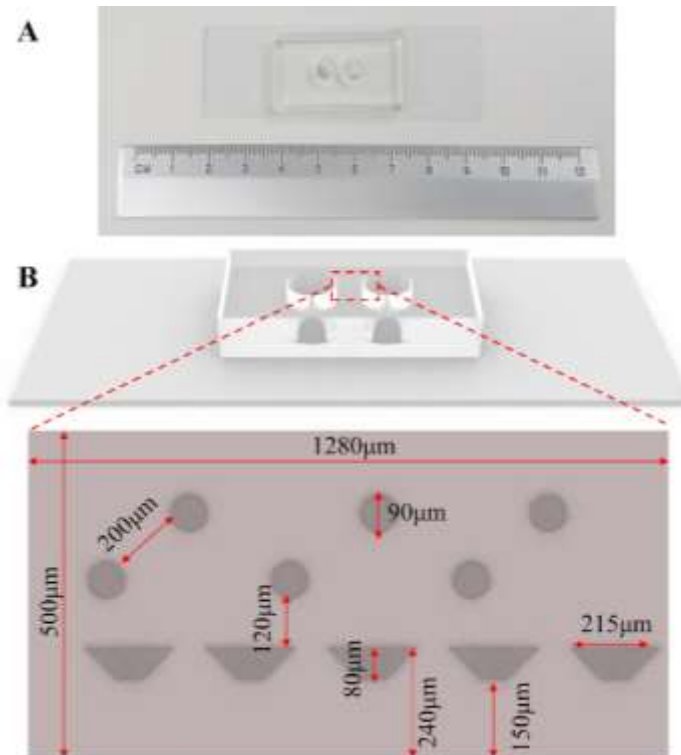


Figure 3.2.1: Microfluidic chip platform for mechanical phenotyping of Glioblastoma at the single-cell level. A. Photograph of the PDMS microfluidic device. B. Model of the microfluidic chip platform, PDMS with inlet and outlet is precisely mounted on the glass ceiling.

3.2.2 *Microfluidic chip preparation and cell culture*

To prepare the microfluidic chip, all reagents and microchips were placed into the incubator for 30 minutes. To eliminate air bubbles inside the microfluidic culture chamber, warm medium was injected using a 200- μl micropipette (Corning, New York, NY, USA) before introducing the cells.

U87 glioma cells were grown as explained above, trypsinized (Pan Biotech, Germany) and resuspended in DMEM medium to obtain 1.6×10^5 cells/ml. Next, 50- μl cell suspension with concentration of 8×10^4 cells/ml were injected into the microfluidic device. The U87 glioma chips were mounted in the incubator and their medium replaced with fresh 40- μl DMEM medium every 24 hours. The U87-C glioma conditional cells were generated by replacing regular DMEM medium with the conditioned medium when the cells were grown

in DMEM medium overnight. Conditioned medium within microfluidic devices were also refreshed once a day. Each experiment was independently performed in triplicate.

3.3 Dielectrophoresis experiments

3.3.1 Device fabrication

The production of 3D carbon-microelectrodes has been described in detail [99]. In short, a two-step photolithography process with SU-8 (Gersteltec, Pully, Switzerland) was applied on a silicon wafer to create the 3D structure of the micro-electrodes.. The 3D carbon-DEP chip has 218 intermediate rows with 14 or 15 electrodes for a total of 3161 electrodes with a height of 100 μm and a diameter of 50 μm . A thin layer of SU-8 was then applied to isolate the planar connectors and make the bottom channel plane. From a 127 mm thick double-sided pressure sensitive adhesive (PSA, Switchmark 212R, Flexcon, Spencer, MA, USA), a 1.8 mm wide, 3.2 cm long channel was cut and glued to a pre-drilled polycarbonate. This arrangement was then manually placed around the carbon-electrode array and closed using a rolling press.

3.3.2 Low Conductive DEP Buffer Preparation

Low conductive DEP buffer was prepared according to previous formula [100], 8.6% sucrose (Product no: LC-4469.1, neoFroxx, Hesse, Germany), 0.3% glucose (CAS Number 59-99-7, Sigma-Aldrich, Darmstadt, in accordance with the pre-specified formula [101], Germany) and 0.1% dilution. Bovine Serum Albumin in distilled water (BSA, Product Code: P06-1391050, PAN-Biotech, Aidenbach, Germany). The conductivity of the final suspension is 20 $\mu\text{S}/\text{cm}$, measured with a conductivity meter (Corning Model 311 Portable Conductivity Meter, Cambridge Scientific Products, Watertown, MA, USA).

3.3.3 Cell preparation

U937 monocyte cells were maintained as described in section 3.1.2 in a humidified incubator at 5% CO_2 - 95% air atmosphere -

Cells were centrifuged at 3000 rpm for 5 minutes to remove remaining culture medium and resuspended twice in DEP buffer. The cell number was determined using a hemocytometer (Catalog No: 0680030, Marienfeld-Superior, Lauda-Königshofen, Germany).

3.3.4 Experimental setup

The experimental setup consisted of a signal generator (Model: GFG-8216A, GW Instek, New Taipei City, Taiwan) and an oscilloscope (Part Number: 54622D, Agilent Technologies, Santa Clara, CA, USA) to create an electric field. An upright microscope (Model: Nikon ME600 Eclipse, Nikon Instruments Inc., Melville, NY, USA) to acquire images (Hewlett-Packard Company, Palo Alto, CA, USA), a programmable syringe pump to flow cells and DEP buffer (Model: NE-1000, New Era Pump Systems Inc, Farmingdale, NY, USA) and our 3D carbon-DEP device. To create a reservoir, we placed two 20–200 μL pipette tips (Manufacturer ID: 3120000917, Eppendorf, Hamburg, Germany) at the inlet and outlet of the microchannel. Tygon micro perforated tube (Manufacturer ID: AAQ02103-CP S-54-HL, Cole-Parmer, Vernon Hills, IL, USA) was used to connect the syringes and microchannels of the 3D carbon-DEP chip.

3.3.5 Experimental procedure

First, the DEP chip was sterilized with 70% Ethanol and then with DI (deionized) water. Next, the 3D carbon-DEP chip was filled with a DEP buffer and all the bubbles on the chip were removed. Cells were then prepared as described above and 40 μl of cell suspension was loaded into the chip using a flow rate of 10 $\mu\text{l}/\text{min}$. When the cells reached the area of the carbon electrodes, the flow was cut off and the cells were seated for 30 seconds. A signal with 20 V_{pp} (peak to peak voltage) and 50 kHz - 1 MHz was applied for the cells in the 3D carbon-DEP device using the function generator [102,103]

3.3.6 Image acquisition and statistical analysis

All images were recorded during the experiments using a 10 \times lens mounted on a Nikon Eclipse vertical optical microscope. We used a VLC software (VideoLAN version 1.8, Paris,

France), to integrate image sequences into movies. Images of cells were analyzed using ImageJ (version 2.0 National Institutes of Health, Rockville, MD, USA). Each image had the location information of the cells for a given frequency. The positions of the cells from the strong pDEP region to the strong nDEP region were rated from 3 to -3. A single cell was monitored for each frequency and the position. The deformation index of the cells are calculated using the measured width and height information of each cell at frequencies varied from 50 Hz to 1MHz.

3.4 Conventional cell culture assays

3.4.1 Growth curve

Once the U87 cells reached 75 to 85% of confluency, cells were trypsinized (Pan Biotech, Germany) and resuspended in fresh DMEM medium with trypan blue dye (Sigma-Aldrich, Darmstadt, Germany). Next, the number of viable cells were counted using a hemocytometer (Marienfeld, Germany). U87 cells were seeded at a density of 1×10^5 cells/well in a 12-well cell culture plate (TPP, Switzerland) and allowed to adhere overnight kept in the incubator. After overnight incubation, three wells were assigned as U87 growth and fed by DMEM medium, while the others were assigned as U87-C and fed by conditioned medium for 8 days in the incubator. Both medium replacement and cell count determinations were performed once every 24 hours for 8 days. To determine the cell numbers, the cells were trypsinized (Pan Biotech, Germany), centrifuged at 1800 rpm for 10 minutes. The cell pellets were collected and suspended in fresh medium with trypan blue dye. Total viable cells were counted using a hemocytometer (Marienfeld, Germany) for both U87 and U87-C growth conditions. Each experiment was independently performed in duplicate. Results were represented by means \pm standard errors.

3.4.2 Wound healing

Wound healing assay was performed in 12-well cell culture plates (TPP, Switzerland). U87 cells were seeded at a density of 5×10^5 cells/ml maintained in 2 ml DMEM medium and allowed to adhere overnight at 37°C, 5% CO₂. Next, 6 wells of U87 culture were grown in regular medium (DMEM medium with 10% FBS and 1% Pen/Strep) while the other 6

wells were maintained in conditioned medium until they become confluent (2 days). Before scratch wound was created in the cell monolayer with a 200- μ l-pipette tip (Eppendorf, Germany), phase-contrast images of the wells were observed using an inverted fluorescent microscope, the Zeiss Axio Observer (Carl Zeiss Axio Observer Z1, Germany) equipped with a 10x objective and the AxioCam Mrc5 camera (Control images). The wells were washed with DMEM to remove the floating cells, 2 ml of either regular or conditioned medium per well were added, the images of the wells were obtained as explained above. The cell migration was observed into the wound area and the images of the wells were acquired at 24 hours. Each experiment was independently performed in duplicate. The wound closure analysis was performed with ImageJ (Version 2.0 National Institutes of Health, Rockville, MD, USA).

3.4.3 *Boyden chamber assay*

Boyden chamber assay was performed in a 6-well plate. Collagen coated Boyden chambers (Transwell-COL, Corning Incorporated, Costar, #3492) were equilibrated by placing them in a well containing 1 ml of media alone (no serum) and adding 1 ml of media alone to the top. Chambers incubated for 2 hours at 37°C and 5% CO₂. Macrophages and glioma cells were prepared as described in 3.4.1. Cell supernatants were resuspended in 5 ml media. 5x10⁵ U87 and 1x10⁶ macrophage cells were mixed and the volume adjusted to 1 ml with media ratios of 2:1 RPMI 1640: DMEM. Cell mixtures are added to the top chamber and incubated at 37°C, 5% CO₂ for 24 hr. The non-invasive cells from the top part of the chamber were gently removed using a cotton tip. Hoechst and propidium iodide staining was performed and chambers maintained in PBS. Image acquisition performed by placing chambers on glass slides.

Experiment groups indicated in Figure 3.4.3:

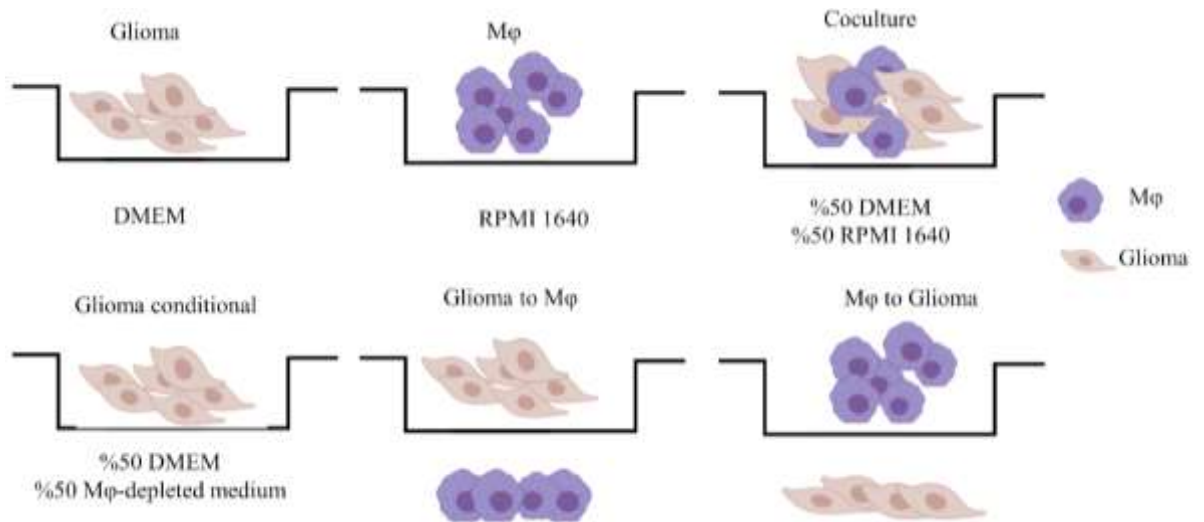


Figure 3.4.3: Cell groups distribution and maintenance conditions in chambers.

Macrophages were labeled with Cell Tracker green CMFDA (Invitrogen #C2925) dye. The nuclei of all cells were labeled with DAPI.

3.4.4 Spheroid formation

Spheroid culture started in 6-well plates as described in the cell culture section. Culture conditions for each group shown in detail in *Table 3.4.4*. The co-culture group showed a high nucleus/cytoplasm ratio and a polygonal morphology from day 7, the same morphology was observed in the glioma group at day 8 and tended to form solid-adhesive spheroids or clumps on the culture surface. U937-derived macrophages cultured as the control group had no obvious change in their morphology.

The area of their spheroids was determined using ImageJ (Version 2.0 National Institutes of Health, Rockville, MD, USA). The number and area of co-culture and glioma spheroids were reported as mean diameter \pm standard deviation.

Table 3.4.4: Spheroid culture properties in 6-well plate

Groups	Glioma	Coculture	Conditional
Cells	Glioma	Glioma & MΦ	Glioma
Media	DMEM	% 50 DMEM % 50 RPMI	% 50 MΦ depleted media and %50 DMEM
# of cells	10000	10000 glioma & 20000 MΦ	10000 glioma

Media change	Daily	Daily	Daily
Imaging	Daily	Daily	Daily
Duration	14 days	14 days	14 days

3.5 Immunostaining and live cell staining

3.5.1 Live cell staining

CellTracker™ Green CMFDA (5-chloromethylfluorescein diacetate, Invitrogen #C2925) and CellTracker™ Red CMTPX (Invitrogen #C34552) live cell marker dyes were used to distinguish macrophages and gliomas in coculture experiments. The lyophilized dye was dissolved in DMSO to make a 10 mM stock solution. The 5uM working solution was prepared by diluting 10 mM solution in serum-free medium (1ul stock solution + 1999ul medium) to the final 5uM working solution. In long-term cultures (4 days or more), the working solution was increased proportionally in the range of 5 to 25 μ M. After the cells were prepared as described in 3.4.1, they were incubated with pre-warmed CMFDA or CMTPX working solution at 37°C for 30 minutes in a serum-free environment. After incubation, the dye-containing supernatant was discarded by centrifugation at 1800 rpm for 10 minutes and the cells were washed by adding PBS and pipetting at low speed. At the end of the second centrifugation, all dye residues were removed, and the cells were cultured.

3.5.2 Immunostaining

All cells were seeded at the same density on 18 mm diameter round coverslips placed in 6-well plates. On the 3rd, 5th, 7th and 14th days of culture, coverslips were fixed in 4% Paraformaldehyde (PFA, Boster BioSciences, Cat No: AR1068) at 4°C for 1 hour. Coverslips were washed on ice with a PBS solution containing 0.5% Tween 20 (Biofroxx, Einhausen, Hessen, Germany). After washing, all coverslips were incubated with PBS containing 0.1% Triton-X100 (Sigma, T8787) and 0.1% Bovine Serum Albumin (BSA, Sigma A2058) for 1 hour at room temperature.

Afterwards, the coverslips are incubated with primary monoclonal antibodies at 4°C overnight. All primary antibody concentrations were adjusted to 1:100 in 2.5% BSA and 0.05% TritonX-100. After washing, coverslips were incubated with secondary antibodies at

a concentration of 1:200 for 1 hour at room temperature, primary & secondary antibody pairs used were listed in Table 3.5.2

All slides were sealed using 1:1 glycerol and PBS after a final wash with DAPI (Life Sciences 33342).

Table 3.5.2: Antibody and their targets in immunostaining experiments.

Primary Antibody	Secondary Antibody	Target
CD68 (ab213363)	goat anti-rabbit Alexa Fluor 594 (ab150080)	M2 type macrophages
CD163 (ab87099)	goat anti-rabbit Alexa Fluor 488 (ab150077)	M2 type macrophages
CD14 (ab181470)	goat anti-mouse Alexa Fluor 488 (ab150113)	M1 type macrophages-monocytes
Vimentin (ab8978)	goat anti-mouse Alexa Fluor 488 (ab150113)	Extracellular matrix
E-cadherin (ab1416)	goat anti-mouse Alexa Fluor 488 (ab150113)	Extracellular matrix & epithelial cells
CD11b (ab52478)	goat anti-mouse Alexa Fluor 488 (ab150113)	M1 type macrophages-monocytes
CD80 (ab225674)	goat anti-rabbit Alexa Fluor 594 (ab150080)	M2 type macrophages
CD11a (ab52895)	goat anti-mouse Alexa Fluor 488 (ab150113)	M1 type macrophages-monocytes

3.5.3 *Imaging*

Live imaging of cells was acquired using ZEN Pro 2.6 software using a Zeiss Axio Observer (Carl Zeiss Axio Observer Z1, Germany) inverted microscope equipped with A-Plan 10x/ 0.25 Ph1, LD Plan-Neofluar 40x/ 0.6 Corr Ph1 Ph2-M27 objectives. The excitation

and emission values for channels were 495nm/519nm, LP 515 nm for FITC, 535nm/617nm LP 590 nm for PI, and 358-410 nm, LP 420 nm for DAPI.

3.5.4 *Confocal imaging*

All immunofluorescent samples were kept at 4°C in the dark after staining and analyzed simultaneously. A Carl-Zeiss LSM 710 Laser Scanning Confocal Microscope equipped with Plan Apochromat 63x/ 1.4 immersion oil DIC M27 and Plan Apochromat 20x/ 0.8 NA objective lenses were used. XY scanning of 1024×1024 pixel images were performed at 8-bit resolution using 405 nm UV Laser diode, 458 nm, 488 nm, 514 nm Multiline Argon laser. A multidimensional scan tool setting was adjusted for imaging spheroids with a 1 µm z-step interval. XY scans of the samples were taken at a pixel distance of 0.27 µm.

The FITC channel of the CD68 and CD14 was set to 1.9 arbitrary unit, AU, while the pinhole was set to 1 AU during acquisition of all channels. Exposure rates of DAPI and FITC channels were 400 mS and 700 mS for CD14, 500 mS and 800 mS for E-cadherin and Vimentin, 450 mS and 700 mS for CD68, 450 mS and 650 mS for CD11a and CD11b, respectively. Red channel exposure ratios are set at 600 mS for CD163 and 800 mS for CD80. The excitation and emission values were 410/517 nm for the red channel, 494/591 nm for the green channel, and 458/561 nm for the blue channel, respectively.

Render images are 3D views of Z-stack images created using Zen 2010 Software. The mean fluorescence intensity of proteins and markers of CD68, CD80, CD163, E-cadherin and Vimentin were measured using the Zen 2010 program and analyzed using GraphPad Prism 5 (Windows Prism 5, version 5).

4 CHAPTER FIVE: CHARACTERIZATION OF HETEROGENEITY USING CONVENTIONAL TECHNIQUES

4.1 Glioma cell proliferation

The growth of glioma cells for 8 days in a 12-well plate using conventional cell culture techniques was obtained based on the hemocytometer count, shown in Figure 4.1. The proliferation of glioma cells for 8 days in a 12-well plate using conventional cell culture techniques shows that cell division occurs most often when glioma is co-cultured with macrophage cells. Cell division shows the slowest proliferation profile in the glioma conditional population. The data in Figure 4.1 are raw data obtained, they are not normalized.

Figure 4.1. and Figure 5.1 shows that the macrophages affect glioma cell morphology directly (in the same medium) or indirectly (paracrine, medium containing the proteins produced by macrophages). Glioma cells developed long branching and stellate morphologies similar to mesenchymal cells in the conditional medium [104].

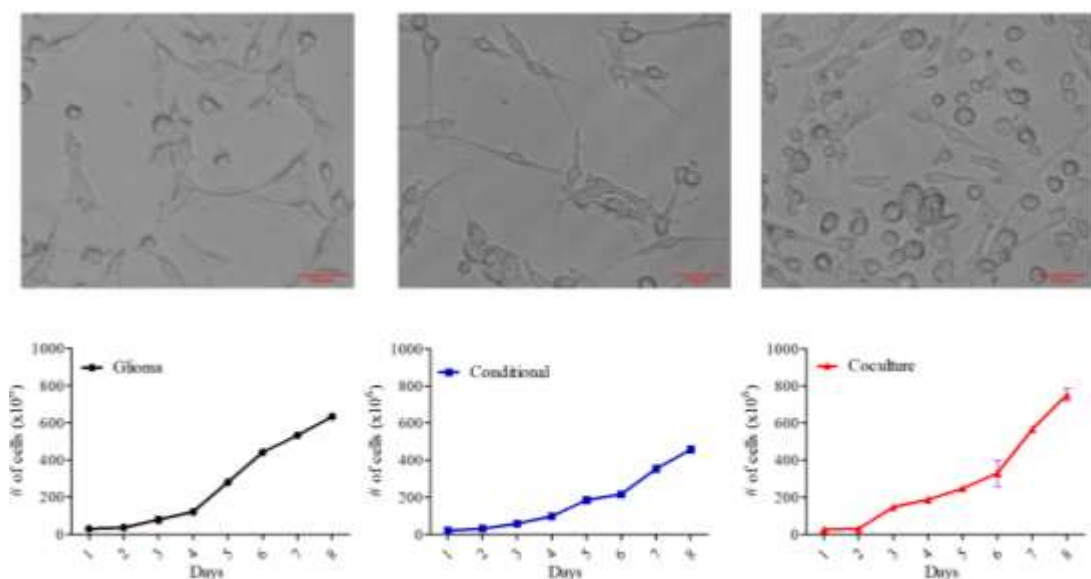


Figure 4.1: Glioma cell proliferation in different maintenance conditions. The scale bar shows 100 μm . The number of cells present the mean \pm standard error for two independent experiments.

4.2 Glioma cell migration

The experimental protocol in a 12-well cell culture plate for the wound healing assay is described in Materials and Methods 3.4.2. During the closure of the wound area on the surface covered by the glioma cells, the orientation of the cells and the culture condition with the highest closure capacity were determined. Of the culture conditions, culturing of glioma cells in DMEM medium and glioma cells in 50% DMEM and 50% macrophages in medium (conditioned medium) was examined. Figure 4.2 shows the degree of wound closure created under these culture conditions after 24 hr and the number of cells that migrated to the wound area. In these images, since the nuclei of the cells are labeled with DAPI, the blue color indicates live cells, and the red color, which is stained with Propidium iodide (PI), indicates dead cells. Yellow lines show the wound area created at 0 hour. The results show the mean \pm standard error of two independent experiments, the statistical difference between the two migration profiles being $p = 0.9051$ [104].

Comparing the migration characteristics of glioma cells in a 12-well cell culture plate under normal growth (100% DMEM) and conditional growth conditions (50% DMEM and 50% RPMI used by macrophage cells), there was no statistical difference in the number of migrating cells under either condition. However, looking at the morphologies, the glioma cells in DMEM medium did not spread as much in the wound area as in the conditional medium, but rather located in the region at the margins of the wound. This showed the tendency of glioma cells to move more in the conditioned medium and to follow a more complex movement profile.

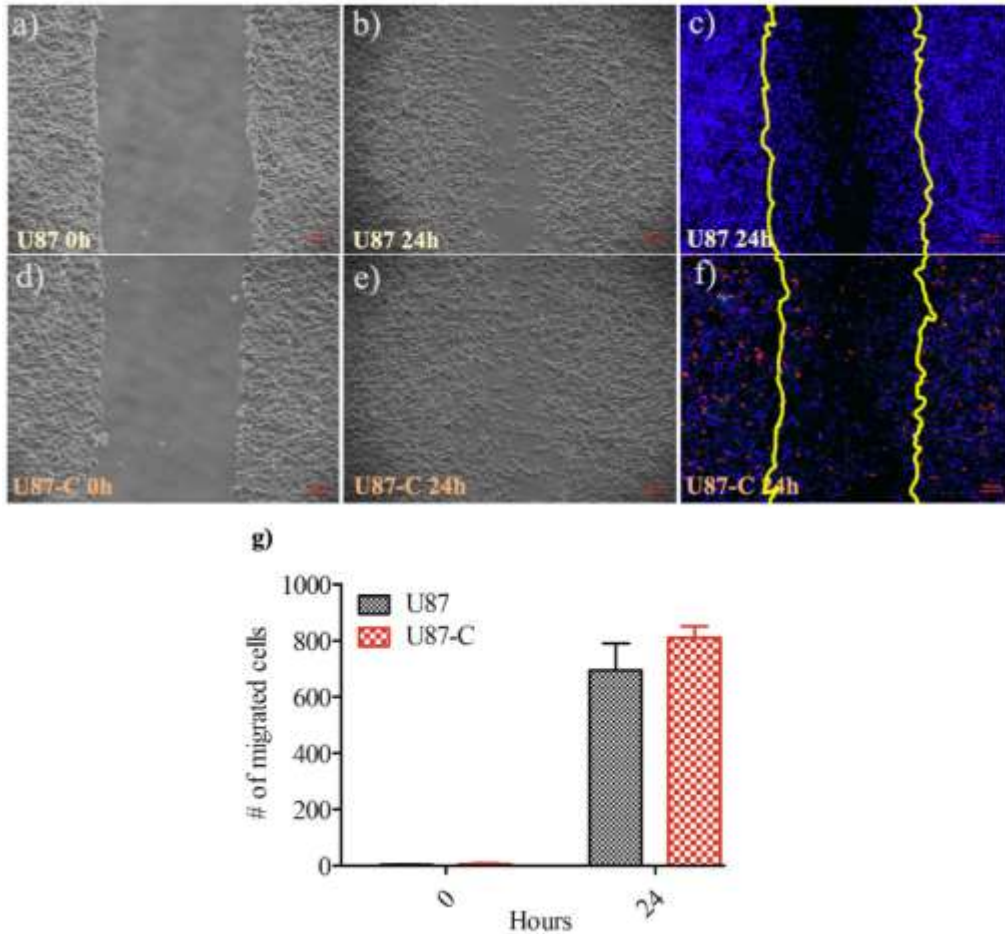


Figure 5.2: Analysis of U87 and U87-C cells migration by the *in vitro* wound-healing assay. The phase images of U87 cells when the (a) wound created at 0 h, (b) phase images of wound closure at 24 h, (c) fluorescence images of wound closure at 24 h, cells labeled with DAPI and PI, yellow lines present the wound area created at 0 h. The same settings applied for U87-C (d–f). The scale bar shows 100 μ m. (g) The number of migrated cells at 0 and 24 h, $p = 0.9051$.

4.3 Glioma-Macrophage coculture and spheroid formation

It was observed that spheroids were formed from day 7 when glioma cancer cells were cultured for 14 days both in 6 and 12-well plates by conventional cell biology methods.

The number of spheroids formed by glioma cancer cells is higher in number when glioma cells are cultured in DMEM medium for 14 days, and in area covered by spheroids when cultured with macrophages (Fig.4.3. d).

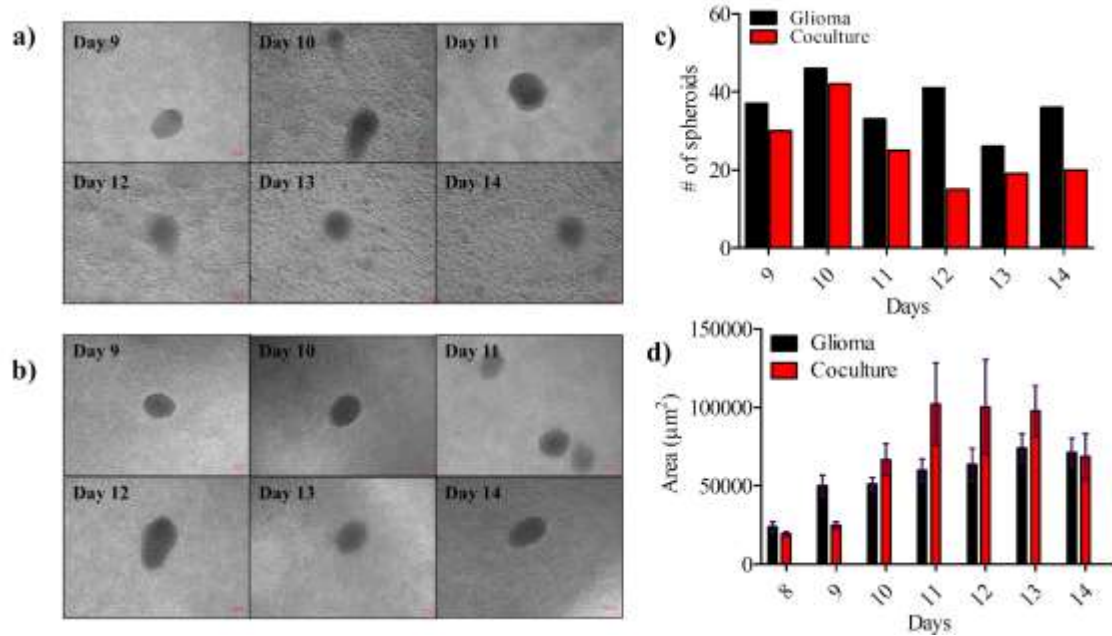


Figure 4.3: Spheroid formation: a) Glioma and b) coculture spheroids between the days of 9 and 14. Quantification of c) spheroid number and d) spheroid area. The number of spheroids and area present the mean \pm standard error for two independent experiments.

4.4 Immunostaining of Glioma and Macrophages

Immunostaining of glioma, conditional and coculture cells on the surface of round coverslips performed on 3, 5, and 7 days. Images of these experiments were obtained using the Olympus BX60 Fluorescence Microscope at 63x magnification. The protein amount arithmetic density values of the obtained immunostaining results were obtained using ImageJ software. One-way analysis of variance Tukey's multiple comparison test was used to analyze these data but no differences were statistically significant at the $p < 0.05$.

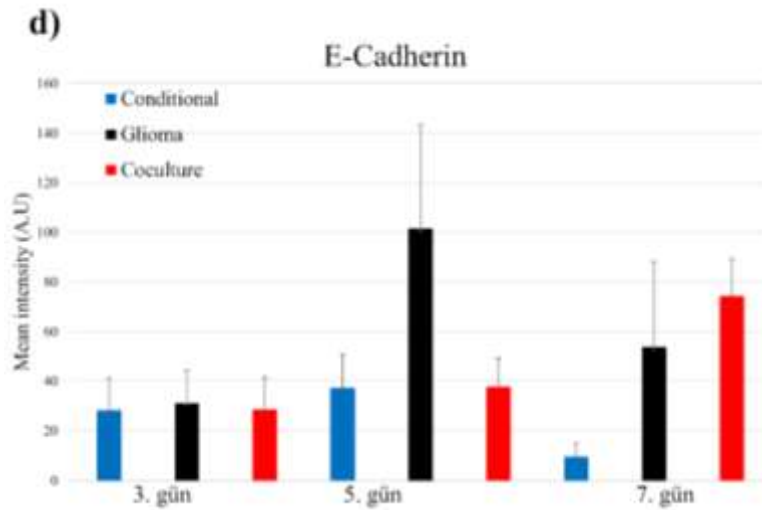
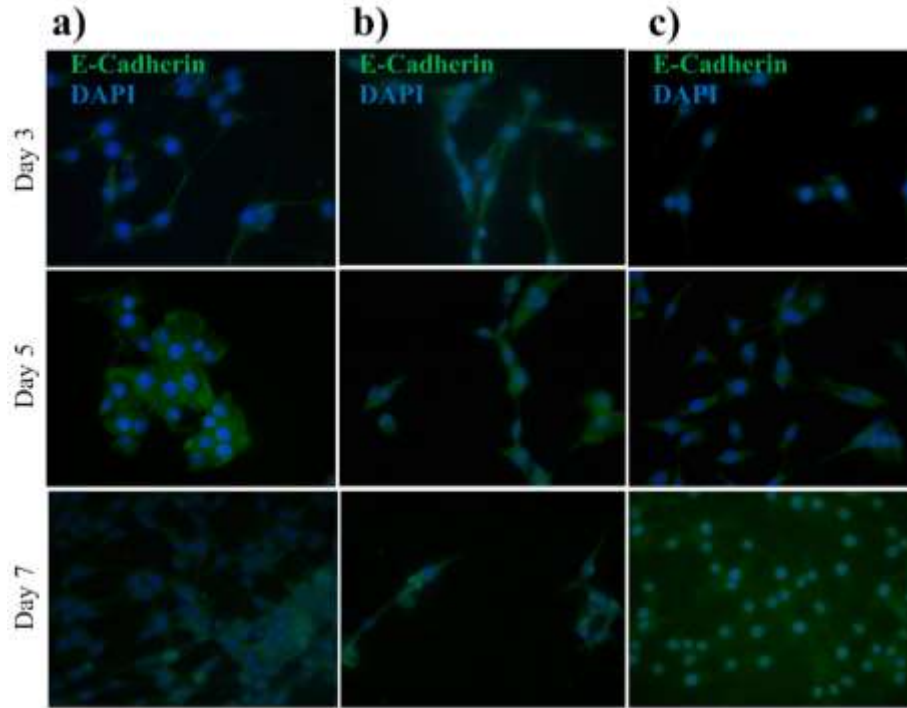


Figure 4.4.1: Comparisons of E-cadherin expression levels.

(a) Immunofluorescence staining of E-cadherin in Glioma, (b) Conditional, (c) coculture groups. AF488 (green) with E-cadherin primary antibody and nuclei counterstained (blue) by DAPI. The scale bar is 25 μm , the magnification is x63. Quantification of (d) E-cadherin expressions of those cells for 3, 5, and 7 days. The one-way analysis of variance Tukey's multiple comparison test was applied.

Expression of E-cadherin protein was the same in all three culture conditions of glioma cells. On day 5, expression in glioma cells slightly increased compared to other days and medium conditions.

Vimentin protein was overexpressed in coculture compared to culture of glioma cells (Fig.4.4.2.d).

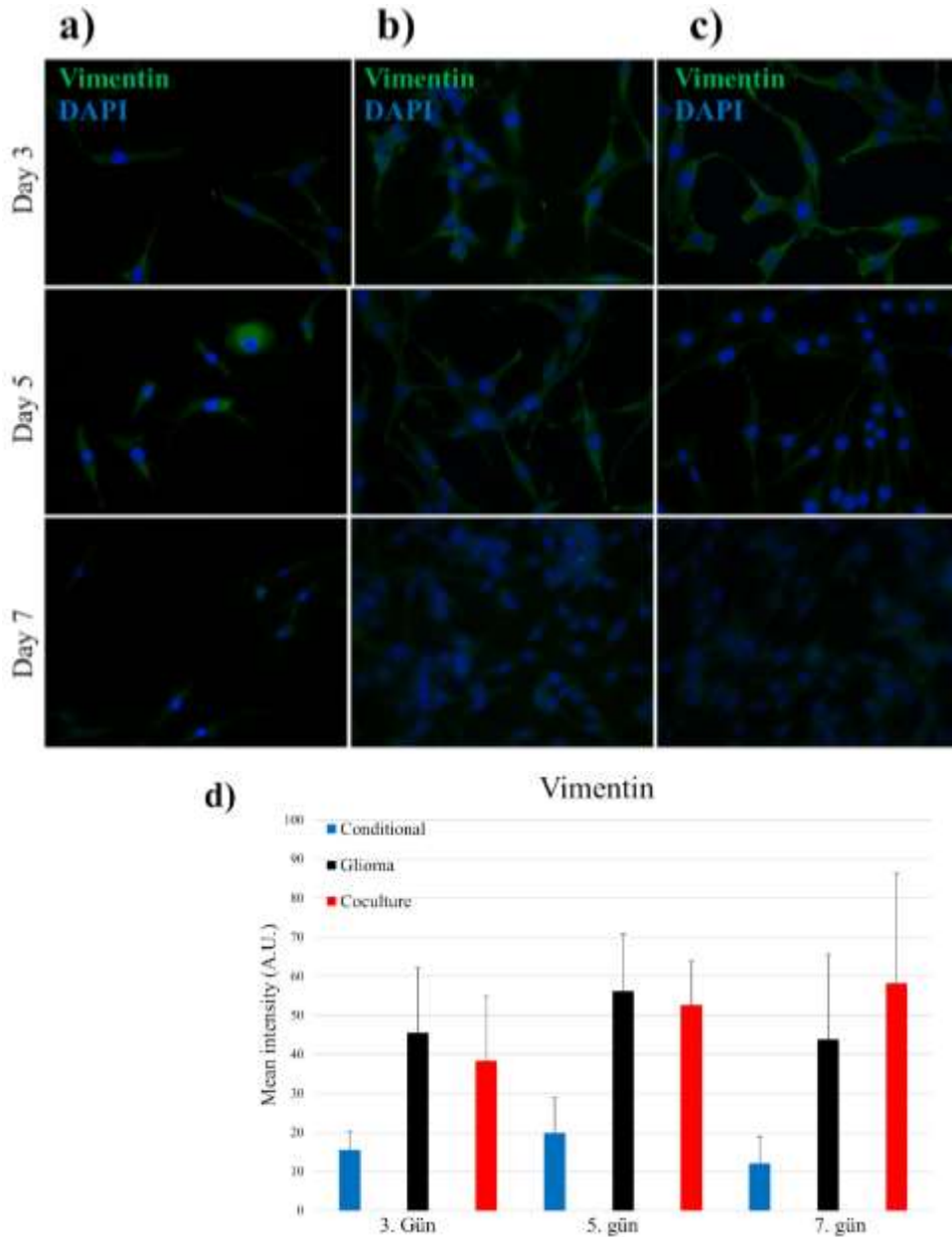


Figure 4.4.2: Comparisons of Vimentin expressions. (a) Immunofluorescence staining of E-cadherin in Glioma, (b) Conditional, (c) coculture groups. AF488 (green) with Vimentin primary antibody and nuclei counterstained (blue) by DAPI. The scale bar is 25 μ m, the

magnification is x63. Quantification of (d) E-cadherin expressions of those cells for 3, 5, and 7 days. The one-way analysis of variance Tukey's multiple comparison test was applied.

In order to examine the TAM characteristics of macrophages, the measurements of the proteins presented in Table 3.5.2 were performed for macrophages. Figure 4.4.3 shows the expression of CD68 (ab213363) and CD163 (ab87099) proteins in RPMI medium of macrophages. The average intensity (pixel) of expression of CD68 and CD163 proteins in RPMI medium by macrophages is 7 a.u and 10 a.u, respectively. High expression of CD68 and CD163 proteins in macrophages indicates conversion of macrophages to M2 type.

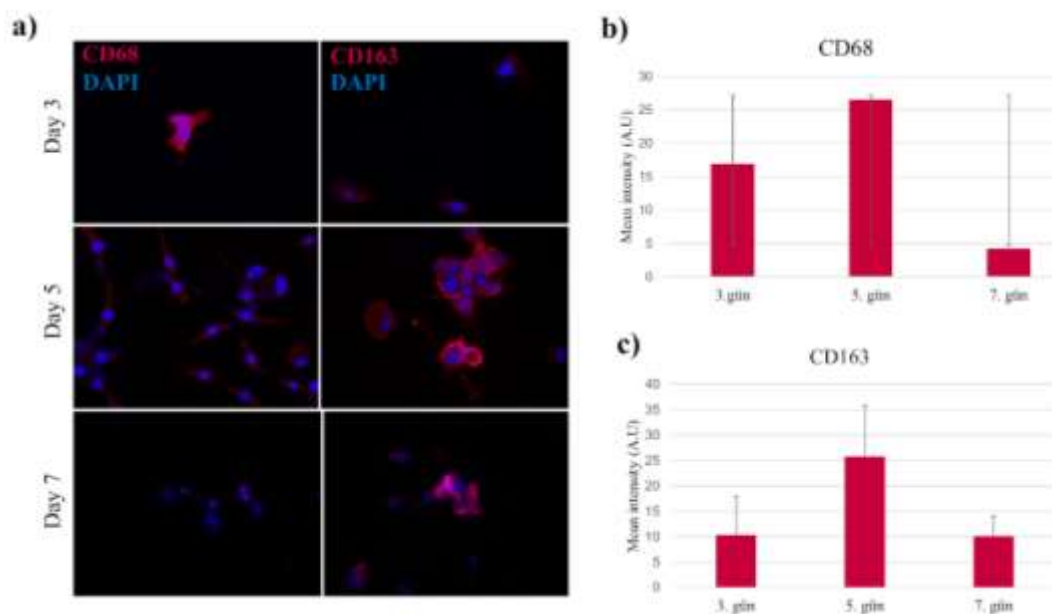


Figure 4.4.3: Comparisons of CD68 and CD163 expressions. (a) Immunofluorescence staining of CD68 and CD163 in macrophages, AF594 (red) with CD68 and CD163 primary antibody and nuclei counterstained (blue) by DAPI. The scale bar is 25 μ m, the magnification is x63. Quantification of (b) CD68 (c) CD163 expressions of macrophages for 3, 5, and 7 days. The one-way analysis of variance Tukey's multiple comparison test was applied.

The expression of CD68 and CD163 proteins in macrophages, especially at day 5, indicated the M2 phenotype. The amounts of these proteins decreased again on the 7th day. The standard errors of the mean values of the measurements are high in the CD68 population. This shows the heterogeneity of the macrophage population and the time-dependent changes in CD68 and CD163 protein expressions of macrophages in this population.

Figure 4.4.4. shows the expression of CD11a (ab52895), CD11b (ab52478) and CD14 (ab181470) proteins at day 3 in glioma and macrophage coculture of macrophages. Amount of CD11a (ab52895), CD11b (ab52478) and CD14 (ab181470) proteins in macrophages indicates conversion of macrophages to M1 type. The results were obtained using the Carl-Zeiss LSM 710 Laser Scanning Confocal Microscope. Image data were not processed because the measurement of the expression of these proteins was very poor.

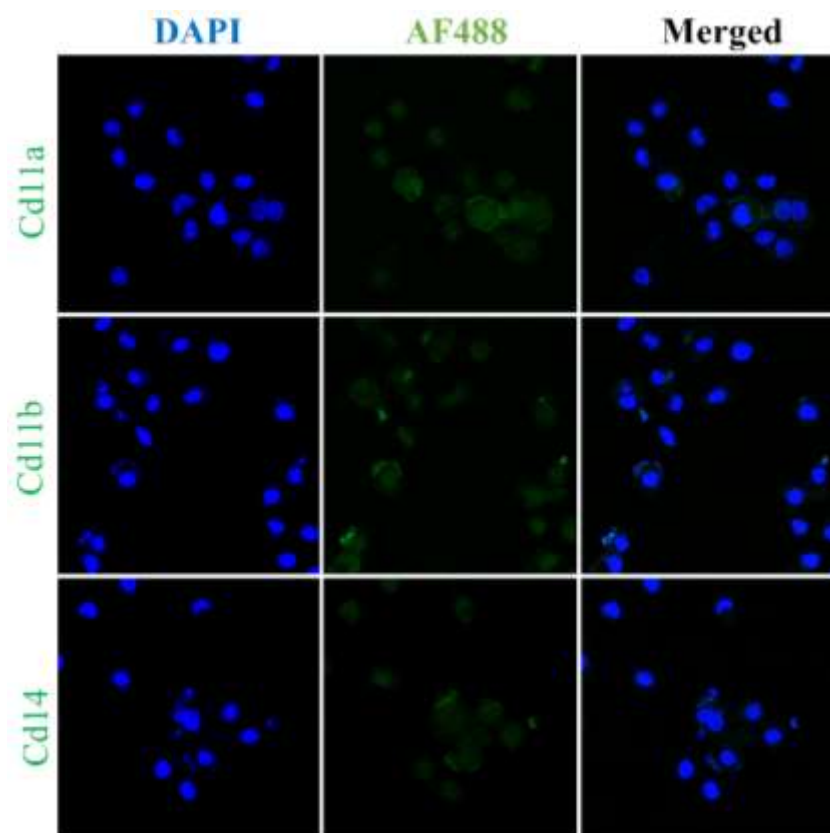


Figure 4.4.4: Immunofluorescence staining of CD11a, CD11b, and CD14 in macrophages. AF488 (green) with CD11a, CD11b, and CD14 primary antibodies and nuclei counterstained (blue) by DAPI. The scale bar is 25 μm , the magnification is x63.

4.5 Immunostaining of spheroids

The propagation of glioma cells in spheroids and expansion in the extracellular matrix were measured by the expression of E-cadherin (ab1416) proteins (green).

Immunostaining of spheroids formed by glioma and coculture cells on day 14 for E-cadherin and CD80 is shown in Figure 4.5.1. After the spheroids were imaged at 20x

magnification, the interior of the spheroid was imaged at 63x. All 3D images are derived from z-stack videos.

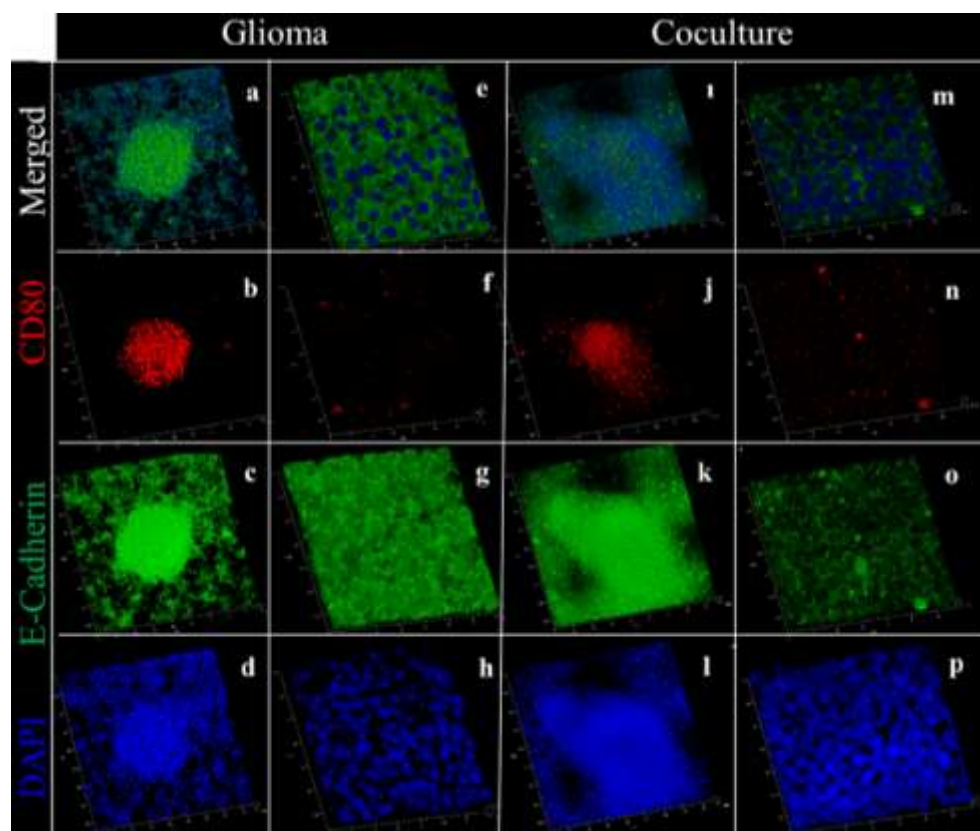


Figure 4.5.1: Comparisons of CD80 and E-Cadherin expressions. (a) Immunofluorescence staining of CD80 and E-Cadherin in Day 14 spheroids, secondary (b), (f), (j), (n) AF594 (red) with CD80 primary and (c), (g), (k), (o) AF488 (green) with E-Cadherin primary antibody and (d), (h), (l), (p) nuclei counterstained (blue) by DAPI. The render images of the spheroid bodies taken with the magnification of 20x (a), (b), (c), (d), (i), (j), (k), (l), zoomed images taken with the magnification of 63x to detect expression inside the spheroids (e), (f), (g), (h), (m), (n), (o), (p).

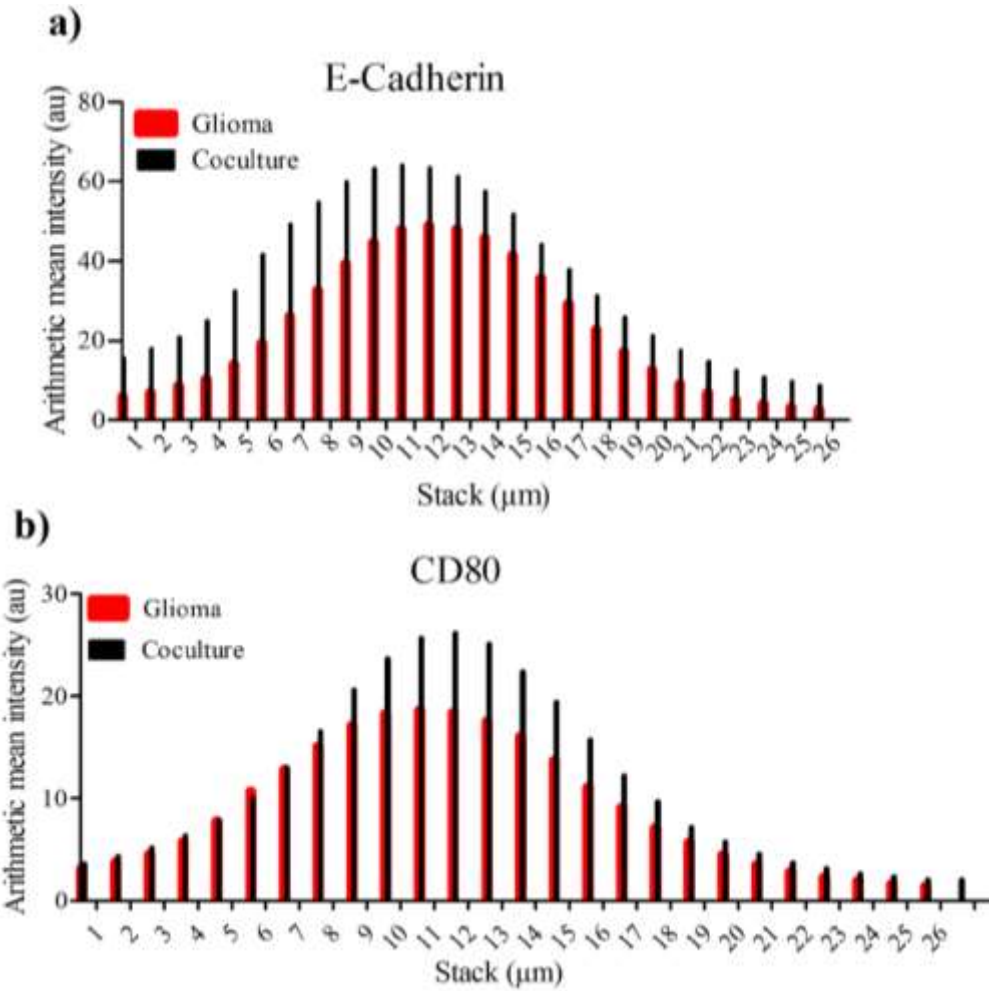


Figure 4.5.2: Quantitative comparisons of CD80 and E-Cadherin expressions. Quantification of (r) E-Cadherin, (s) CD80 expressions of glioma and coculture in Day14.

Immunostaining of spheroids formed by glioma and coculture cells on day 14 for Vimentin and CD163 is shown in Figure 4.5.3. After the spheroids were imaged at 20x magnification, the interior of the spheroid was imaged at 63x. All 3D images are derived from z-stack videos.

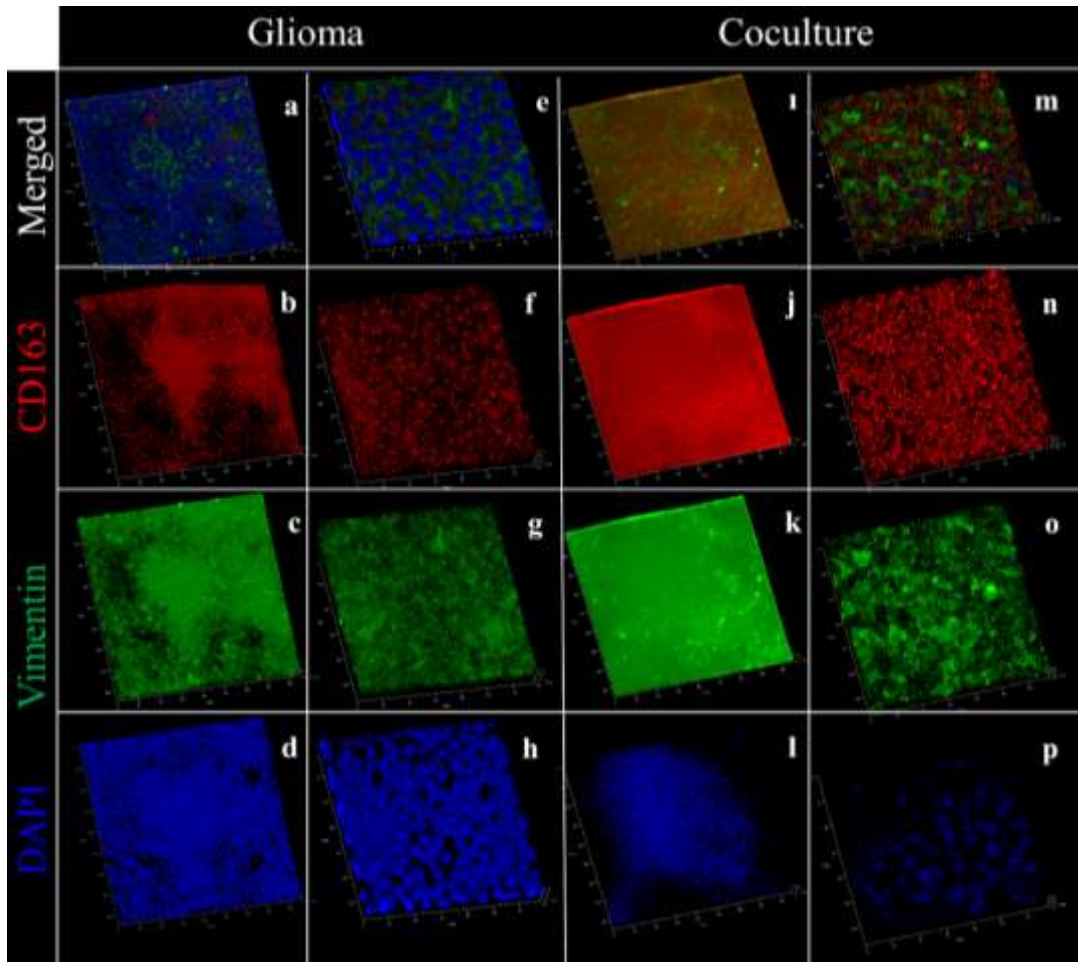


Figure 4.5.3: Comparisons of CD163 and Vimentin expressions. (a) Immunofluorescence staining of CD163 and Vimentin in Day 14 spheroids, secondary (B), (f), (j), (n) AF594 (red) with CD80 primary and (c), (g), (k), (o) AF488 (green) with Vimentin primary antibody and (d), (h), (l), (p) nuclei counterstained (blue) by DAPI. The render images of the sferoid bodies taken with the magnification of 20x (a), (b), (c), (d), (i), (j), (k), (l), zoomed images taken with the magnification of 63x to detect expression inside the spheroids (e), (f), (g), (h), (m), (n), (o), (p).

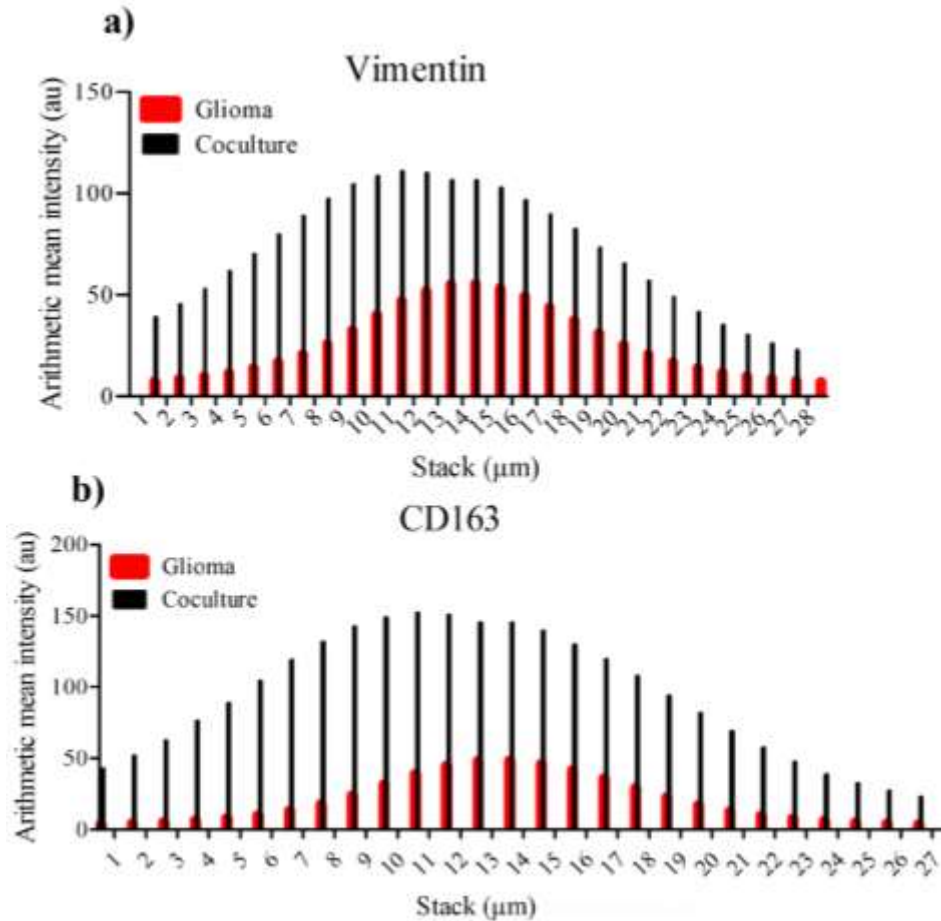


Figure 4.5.4: Quantitative comparisons of CD163 and Vimentin expressions. Quantification of (r) Vimentin, (s) CD163 expressions of glioma and coculture in Day14.

E-cadherin-CD80 and Vimentin-CD163 protein amounts were converted into quantitative data using confocal microscope images (Figures 4.5.2 and 4.5.4). From the obtained z-stack data, these proteins were most measured in the center of the tumor. The measurement of proteins inside the tumor conforms to the Gaussian distribution. E-cadherin and CD80 proteins were measured slightly more in glioma and macrophage dual culture than in glioma culture alone, but the measured values were not high. Vimentin and CD163 proteins were measured more in coculture. While vimentin was accumulated more on the distal surface of the spheroids in glioma alone, such a distribution was not observed in coculture.

CD68 was also measured more in glioma and macrophage cultured spheroids (Fig.4.5.5). CD68 mostly localized within the hypoxic region of the spheroids in glioma alone while it was distributed along the surrounding cells in the coculture group.

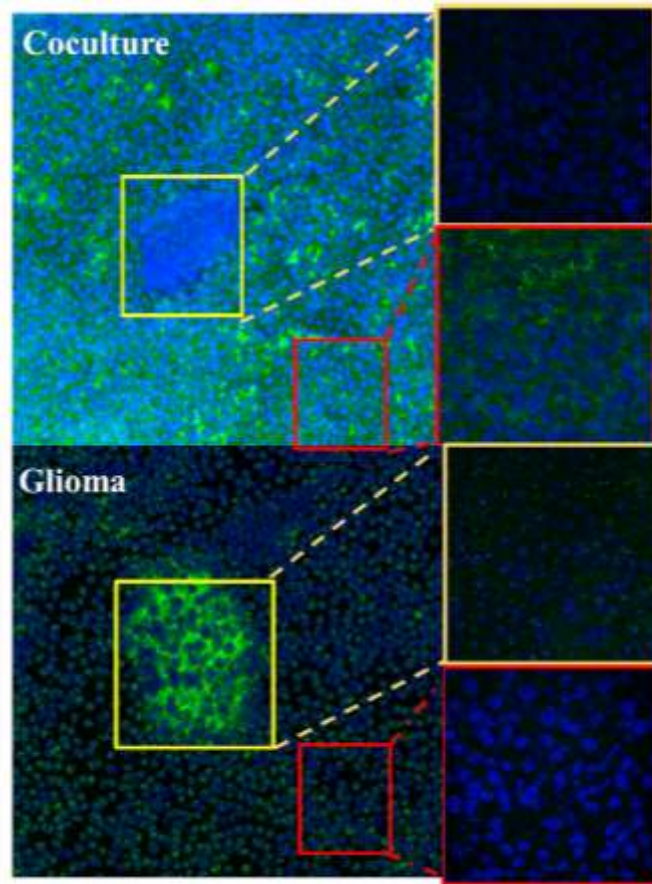


Figure 4.5.5: Comparisons of CD68 localizations in glioma and coculture. (a) Immunofluorescence staining of CD68 in Day 14 spheroids, AF488 (green) with CD68 primary antibody and (nuclei counterstained (blue) by DAPI. The render images of the spheroid bodies taken with the magnification of 20x, zoomed images inside (yellow) and outside (red) of the spheroids taken with the magnification of 63x in both coculture and glioma.

Immunostaining experiment results showed that centers of spheroids formed in both glioma alone and coculture were more aggressive and invasive. Heterogeneity of glioma cells was observed both inside and outside the spheroids. High expression of Vimentin protein in coculture showed that glioma cells in these spheroids were more aggressive. High expression of CD163 and CD68 proteins in spheroids indicates that macrophages acquire M2-type features. However, as stated in the literature, the expressions of these markers are not

sufficient and reliable to subdivide TAMs [107]. It was observed that glioma cells also produced these markers, especially when negative controls of macrophage signs were controlled with glioma spheroids [108].

4.6 Boyden Chamber Assay

Cell groups were placed into the chambers as described in Material & Method 3.4.3. At the end of 24 hours, cells invaded through collagen pores were counted by staining with DAPI. Cells that could not migrate were removed using a cotton stick to avoid interfering with the results. Green and DAPI-stained macrophages and only DAPI-stained gliomas shown in the figure were counted using ImageJ.

Boyden chamber migration experiment clearly suggested the glioma conditional has the highest migration potential and the gliomas when cultured with macrophage still have significantly higher migration properties compared to the glioma alone (Fig.4.6).

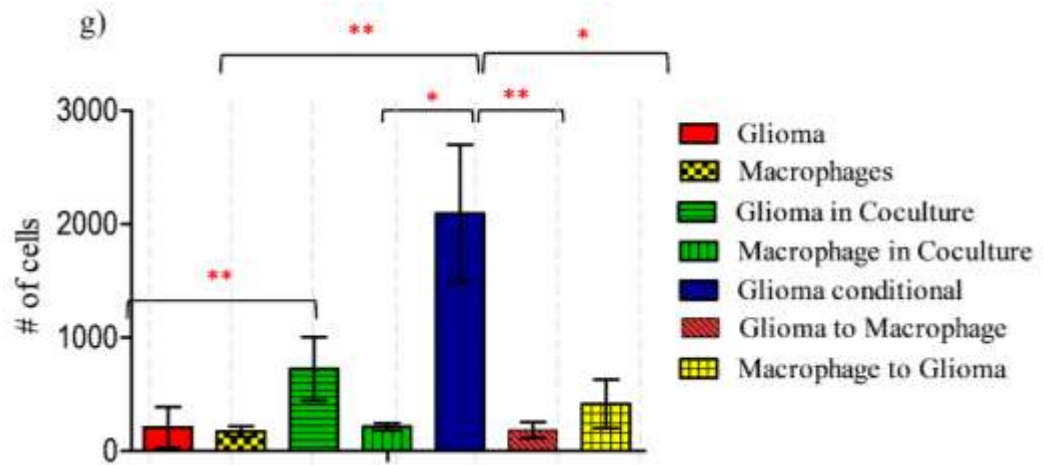
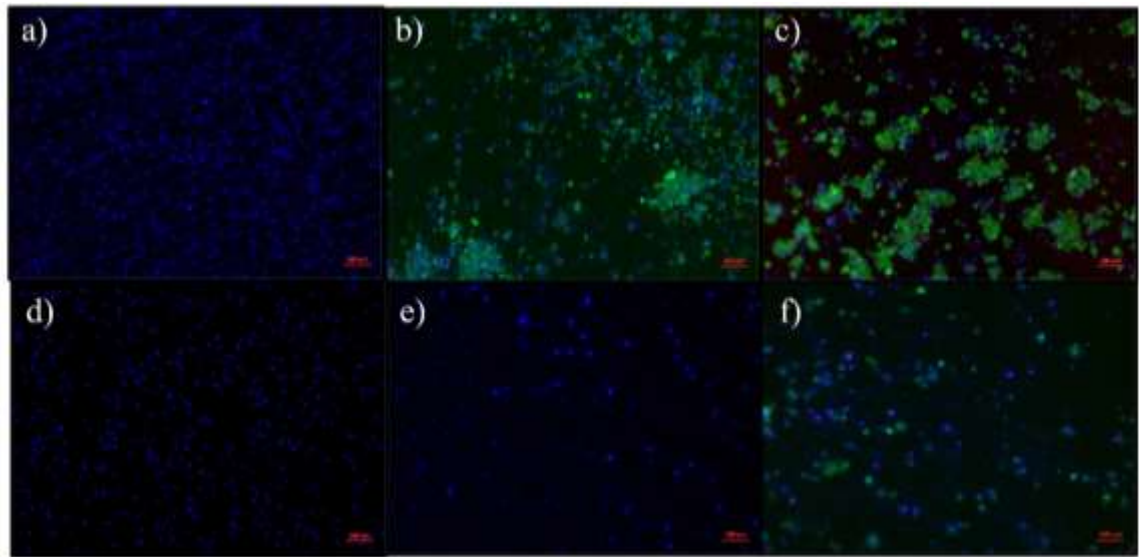


Figure 4.6: Comparisons of cell migration in Boyden chambers. (a) Cells invaded through Boyden chambers (a) Glioma, (b) Macrophages, (c) Coculture, (d) Conditional, (e) Glioma attracting to macrophages, and (f) Macrophages attracting to glioma cells. CMFDA (green) labelled macrophages with nuclei counterstained (blue) by DAPI. The scale bar is 100 μ m, the magnification is 20x.

5 CHAPTER FOUR: CHARACTERIZATION OF HETEROGENEITY in MICROFABRICATED TOOLS

5.1 Comparison of traditional and microfluidic cell culture of glioma

Growth of U87 and U87-C cells was investigated in microfluidic culture. Upon introducing the cells into the microchambers, the cells adhered to the surface of the microfluidic chip overnight. The cellular growth is imaged for five days using the phase channel at twelve hours intervals. The obtained images were quantified to determine the growth rate of the cells in the microfluidic cell culture platform. Figure 5.1 shows the growth of the U87 maintained in DMEM and U87-C maintained in 50% macrophage used RPMI-1640 and 50% DMEM.

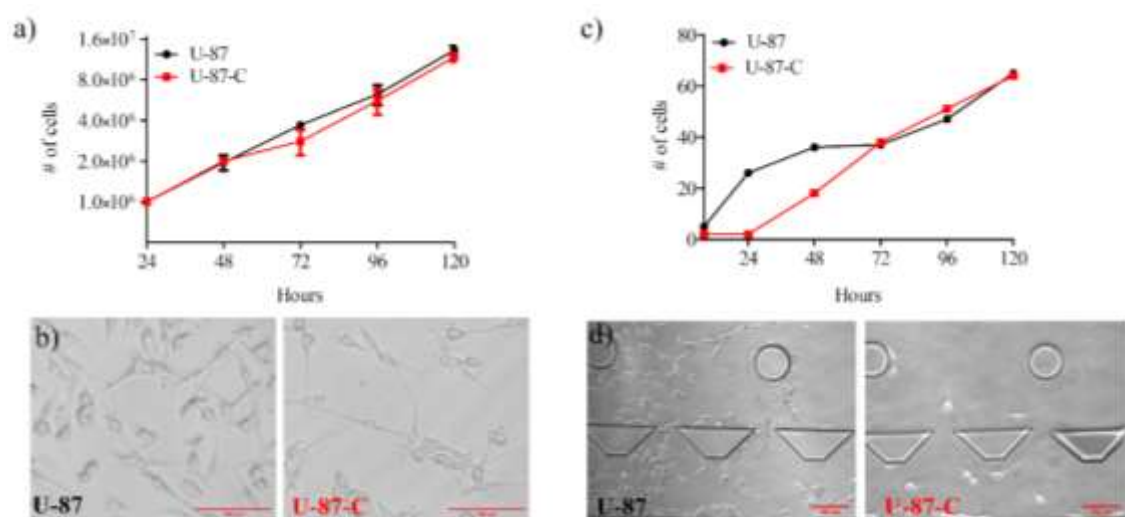


Figure 5.1: Growth comparison. Glioma cells were grown in DMEM medium (U87) and in 50% DMEM and 50% macrophage-depleted medium (U87-C) in the 6-well culture dish and microfluidic platform. (a) The number of viable cells for five days in a 6-well plate, (b) the micrographs of U87 and U87-C cells for a 96-h growth. The scale bar shows 20 μm . (c) The number of viable cells for five days in the microfluidic device, (d) micrographs of glioma cells for the 96-h growth. The scale bar shows 100 μm . The number of cells present the mean \pm standard error for two independent experiments.

5.2 Single-cell migration in microfluidic device

The single cell mobility was serially investigated with an inverted microscope. All cells were manually analyzed using open-access ImageJ software (Version 2.0 National Institutes of Health, Rockville, MD, USA). 40 cells were followed, and their positions were recorded at 12-hour intervals. The y-axis and x-axis determine the vectoral orientation of cells; the microfluidic chip is divided into four parts from left to right plain as “-x, +y”, “+x, +y”, “-x, -y” and “+x, -y”. The intersected point for x and y lines is the reference point for all time intervals and the extended image shows the targeted cell that is tracked at different time intervals.

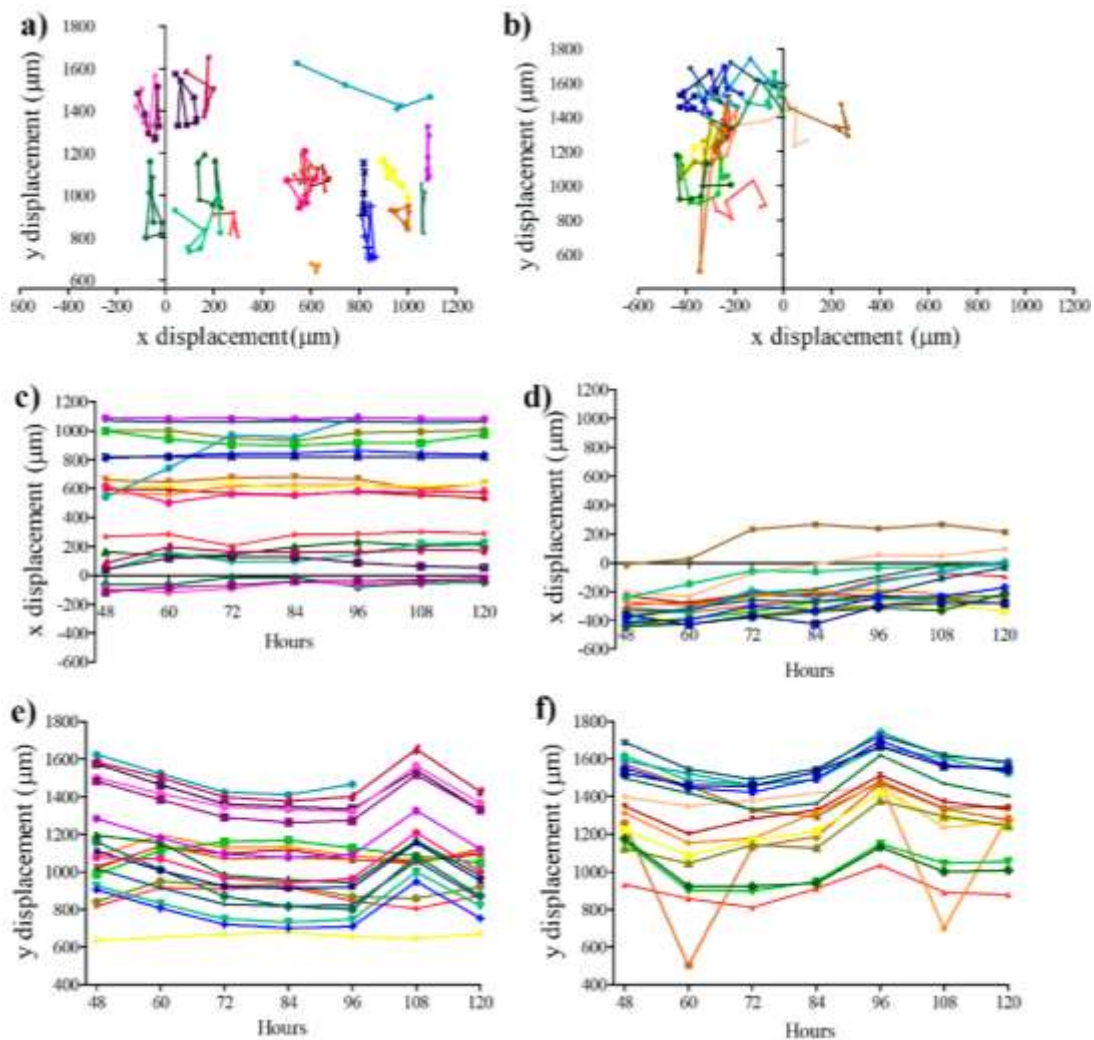


Figure 5.2: Migration of single cells in the microfluidic cell culture chamber. Coordinates of the cells in the microfluidic cell culture device were measured every 12 hours between 48

and 120 hours. Movement of the U87 cells (a) at x-y axes (b) on the x-axis, (c) on the y-axis. Movement of the U87-C cells (d) at x-y axes, (e) on the x-axis, (f) on the y-axis. The number of analyzed cells for each group is 20. U87 indicates that cells cultured in DMEM medium, U87-C defines the cells grown in 50% DMEM and 50% macrophage-used RPMI medium. Each color represents the single cells and color coding was consistent in each group.

5.3 Glioma deformation

The deformation was calculated by manually measuring the area and perimeter of 40 U87 and U87-C cells at 12-hour intervals from 48th hour to 120th hour. The single cell deformation values of each cell were calculated using Eq.4 [105], where Area is the surface area of cell, Perimeter represents the path that encompasses the cell surface:

$$D = 1 - \frac{2\sqrt{\pi Area}}{Perimeter} \quad (4)$$

The cell diameter and deformation were measured manually from ImageJ software (Version 2.0 National Institutes of Health, Rockville, MD, USA). Cell diameter was calculated during analysis from measured surface area [105].

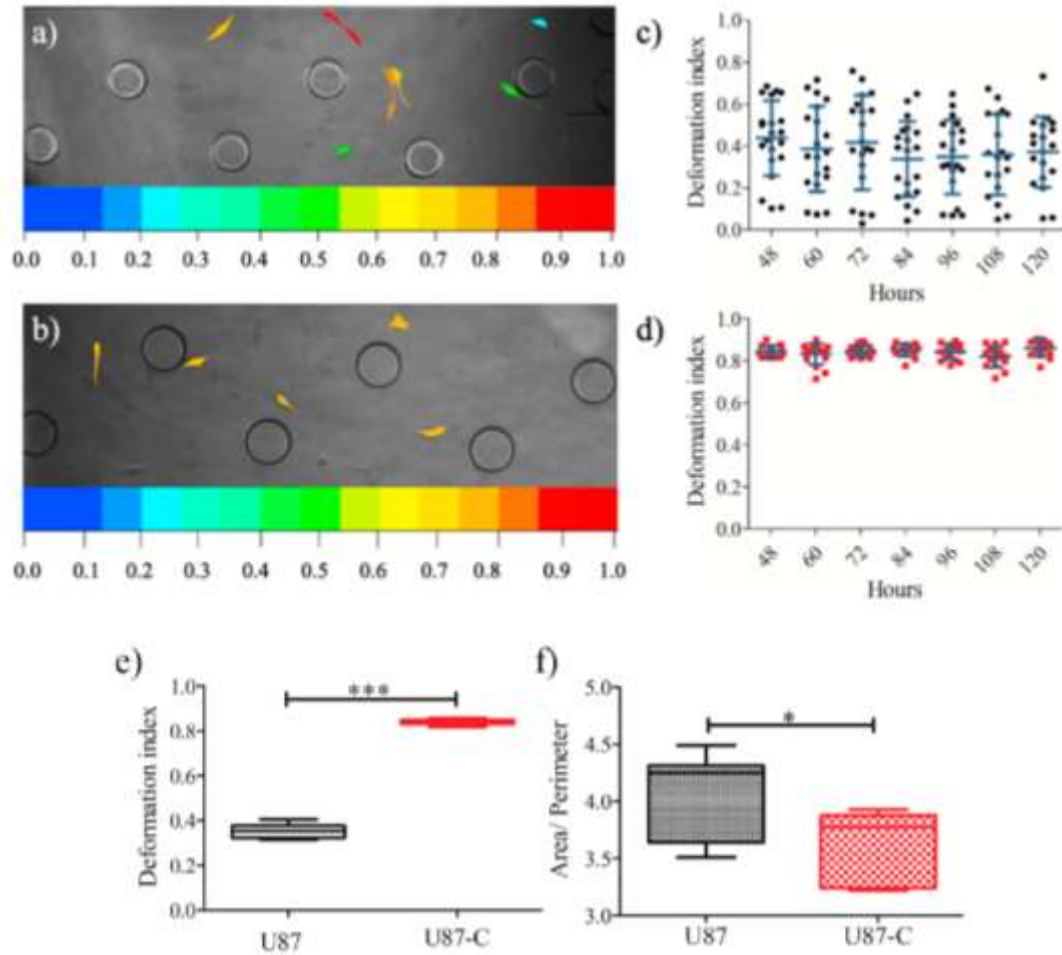


Figure 5.3: Deformation indexes of the cells in the microfluidic device. The phase images of the cells with a colorimetric deformation scale, the range of deformability from coolest colors (blue: 0) to warm colors (red:1) represent enhanced deformability indexed (a) U87 population, (b) U87-C population. The deformation indexes of 20 glioma cells between 48- and 120-h (c) for U87 population, (d) for U87-C population. The data presents the mean \pm standard error. (e) Deformation indexes differences between U87 and U87-C. Student's two-tailed t-test was applied, $p < 0.0001$. (f) Differences of the area to perimeter ratio, p-value is 0.0258. * and *** implies for $p < 0.05$ and $p < 0.0001$, respectively.

5.4 Migration velocity

We measured the velocity of three glioma cells, shown with red, blue, and yellow arrows frame to frame, to compare the change in their velocities, Fig.5.4.1. When cells started to

migrate along microfluidic channel, they show higher speed on Y-axis (Fig.5.4.1.C) compared to X-axis (Fig.5.4.1.B).

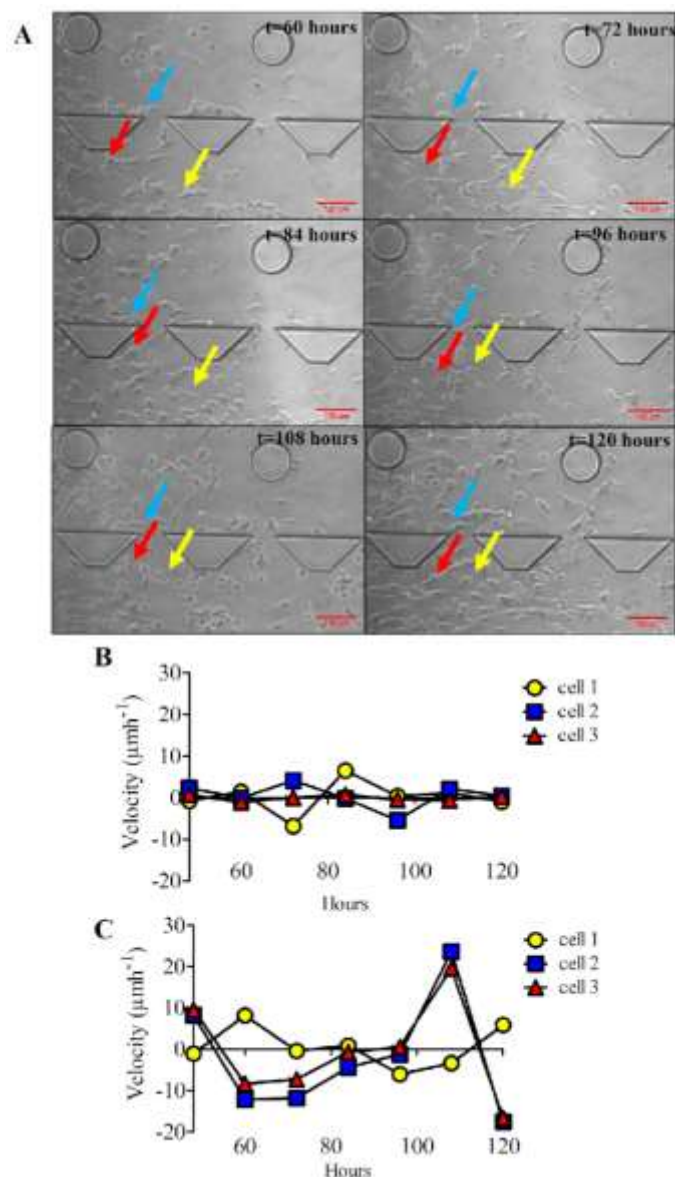


Figure 5.4.1: Velocity changes for the single glioma cells. A) Micrographs of a microfluidic channel with labelled U87 cells that show motion and velocity of cells for 120 hours at 12 hours intervals. B) The change in the velocity for the labelled cells on X-axis and C) Y-axis.

Figure 5.4.2 presents the changes of velocity on the x-y axis for U87 (Fig.5.4.2. A, B) and U87-C (Fig. 5.4.2.C,D) groups. Migration of the cells was demonstrated on the x-axes (Fig. 5.4.2.A, C) and the y-axes (Fig. 5.4.2. B, D). The migration velocities of the U87 cells were

lower in comparison to U87-C. The velocity range of the U87 cell population was smaller (-18 μm to 23 μm) than the U87-C cell population (-64 μm to 136 μm) on y-axis.

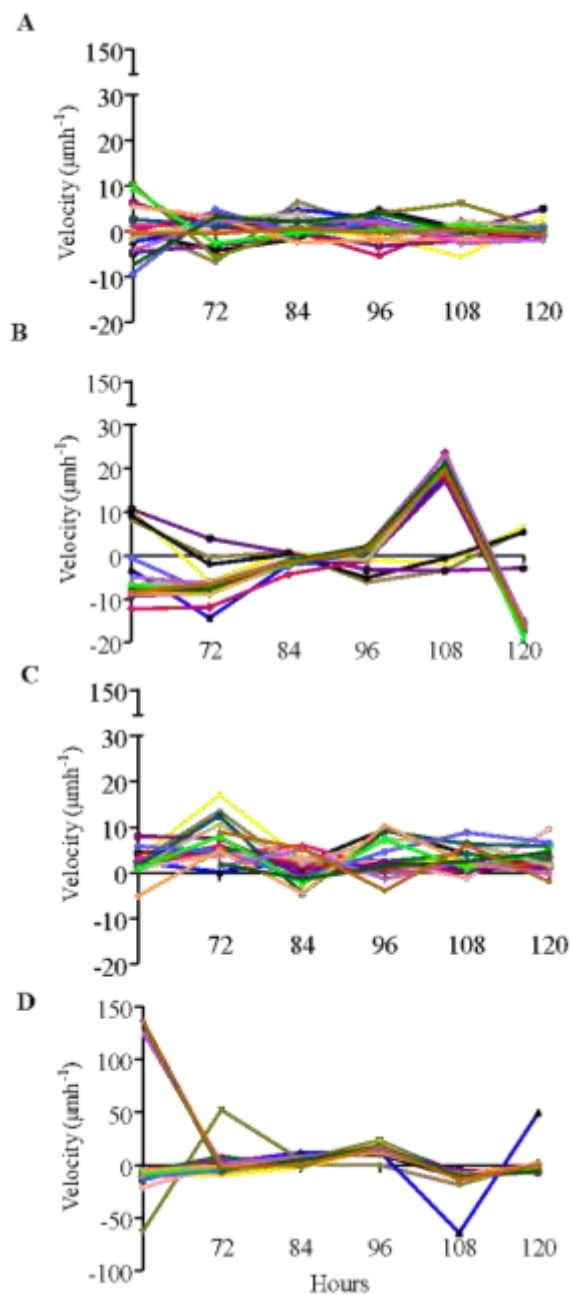


Figure 5.4.2: The velocity of glioma cells in the microfluidic cell culture chamber. The velocity of the cells in the microfluidic cell culture device was calculated every 12 hours between 60 and 120 hours. A) Movement of the U87 cells cultured in DMEM medium on the x-axis, and C) on the y-axis. C) Movement of the U87-C cells grown in 50% DMEM and

50% macrophage used RPMI medium on the x-axis, and D) on the y-axis. Each color represents the single cells and color-coding was consistent in each group.

U87 cells maintained in the regular medium, the cells average velocity in varying time showed a uniform trend compared to the U87-C group where U87 cells were grown in 50% DMEM and 50% macrophage depleted RPMI (Fig.5.C, D).

After evaluating the positions of single cells in the microfluidic device, area and circumference measurements of 40 cells from glioma and conditional glioma populations were determined. Images of the cells were acquired every 12 hours between 60 hours and 120 hours. The perimeter and diameter differences of these two groups were shown in Figure 5.4.3. Figure 5.4.3.C shows that the velocity of the U87-C population is greater than the U87 population significantly according to the Student's two-tailed t-test ($p=0,0097$).

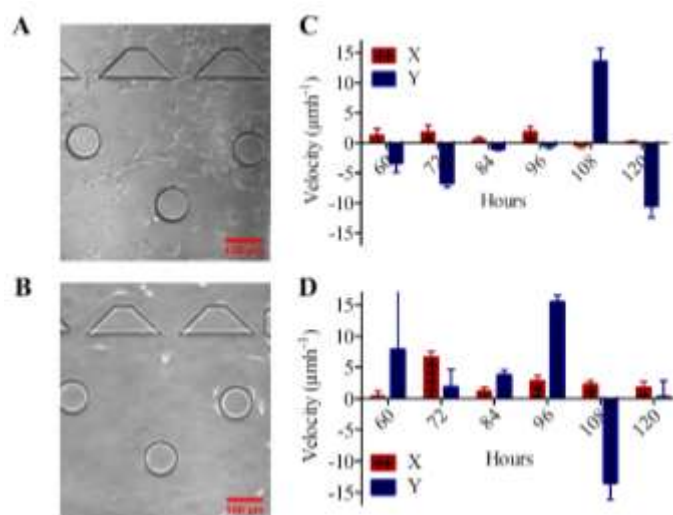


Figure 5.4.3: The average velocity of glioma population under different maintenance conditions. The number of 40 glioma cells analyzed from 60 hours to 120 hours A) under basal maintenance conditions, U87, and C) basal culture supplemented with macrophage depleted medium (1:1 ratio), U87-C. B) The average velocity for U87 cells and D) U87-C cells, represented with mean \pm standard deviation.

5.5 Dielectrophoretic deformation and dielectric responses of Monocyte and Macrophages

Fig.5.5.1. b demonstrates the dielectrophoretic behavior of the U937 monocytes. Monocyte cells experienced nDEP to pDEP forces with increasing frequencies. The

crossover frequencies of monocytes were between 100 kHz to 200 kHz. The uniformity of pDEP responses of the monocytes was improved with increasing frequencies (200 kHz - 1 MHz, the strongest nDEP (-3, dark blue), the strongest pDEP (3, red). On the other hand, the U937-differentiated macrophage cells mostly exhibited pDEP behavior (warm colors yellow-red colors), their weak crossover frequency was around 50 kHz-100 kHz (green), Fig.5.5.1.c. The fraction of cells which immediately presented pDEP response was greater (16 cells) than the nDEP ones (9 cells). The number of nDEP experienced cells were not broadly changed. Since most of the macrophage cells immediately showed pDEP behavior and attracted by the strong dielectrophoretic forces generated by 3D-carbon electrodes, the number of analyzed cells in Fig.5.5.1.c is limited to 20 cells.

The monocyte population showed smooth nDEP (blue) to crossover (green) and crossover to pDEP (red) transition as a whole monocyte population as shown in Fig.5.5.1.b. On the other hand, the macrophage population exhibited more likely a bimodal distribution that is either the macrophage cells were in nDEP (blue) or pDEP (red) in comparison to the monocyte population, Fig.5.5.1. c. Therefore, the dielectric movement of the U937-differentiated macrophages showed more heterogeneous population responses than the U937 monocyte population which is the originals of U937-differentiated macrophages.

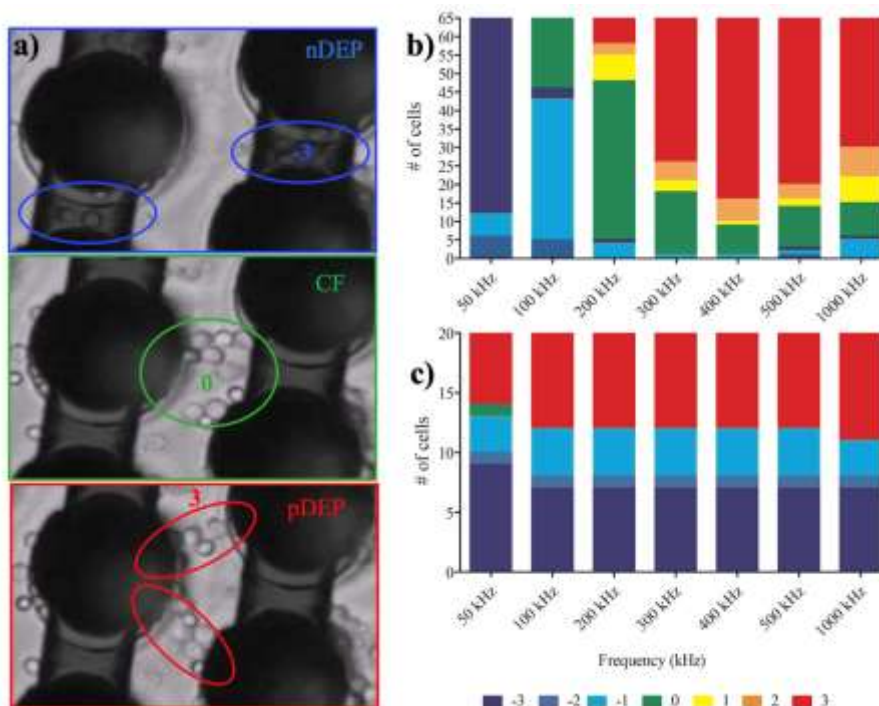


Figure 5.5.1: Dielectrophoretic responses of monocytes and macrophages: (a) Positions of the cells in the electrode array when they are influenced by nDEP, crossover frequency (CF) and pDEP, respectively; (b) Translational movement of U937 monocytes under 20 V_{pp}, 50 kHz–1 MHz nonuniform AC field; (c) Translational movement of U937-differentiated macrophages under 10 V_{pp}, 50 kHz–1 MHz nonuniform AC field. The cool colors show the number of nDEP- behaved cells due to repelling DEP forces while the warm colors demonstrate pDEP-responded cells owing to attractive DEP forces. Zero means the crossover frequency with zero movements, which is coded in green color. n = 80 for monocytes, n = 30 for macrophages.

Fig.5.5.2 compares the dielectrophoretic responses of the U937 monocytes and U937-differentiated macrophages. The macrophages moved from the nDEP region to pDEP region when 50-100 kHz, 20 V_{pp} was applied. The monocytes experienced nDEP to pDEP transition when 100-200 kHz, 10 V_{pp} was provided. When both the monocyte and macrophage populations exhibited strong pDEP forces at 1 MHz, there was a significant difference with $p < 0.05$ between the trapping regions of the cells in the strong pDEP according to students t-test, Fig.5.5.2. This result may show that the interfacial polarization difference between the cytoplasm and plasma membrane can be stronger for macrophages than monocytes (Huang et al., 1996). Therefore, the observed macrophage dielectric properties at 1 MHz can be related to both membrane and cytoplasm properties of macrophages, whereas the membrane features might dominate for the monocyte dielectric properties at 1 MHz. These varying biophysical properties between monocytes and macrophages might explain their distinct trapping regions inside the 3D-carbon DEP device.

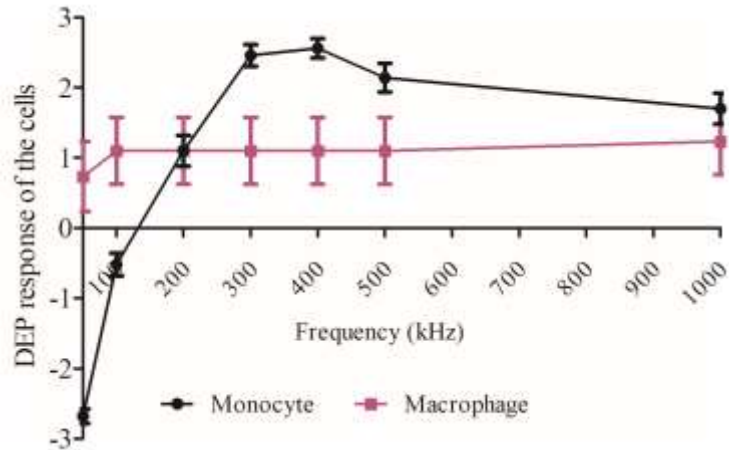


Figure 5.5.2: Comparison between the DEP movement of monocyte and macrophage cells. The magnitude of movement is categorized as very strong (3), strong (2), and weak forces (1). The “-” sign refers to nDEP. Measurements are the mean and error. $n = 50$ for monocytes, $n = 30$ for macrophages.

Fig. 5.5.3, as a representative, shows the deformation of single individual monocytes in the presences of DEP forces. We measured the height and width of three monocytes frame-by-frame to follow the change of their deformation index in varying DEP forces. The same color address same monocyte cell at the given frequencies, Fig. 5.5.3.a.

Fig. 5.5.3.b. displays the change of monocyte deformation index (labelled in Fig. 5.5.3.a.). The dynamic changes in monocyte localization according to applied dielectrophoretic forces clearly shows a qualitatively different behavior of monocytes causes scattered distribution at higher frequencies.

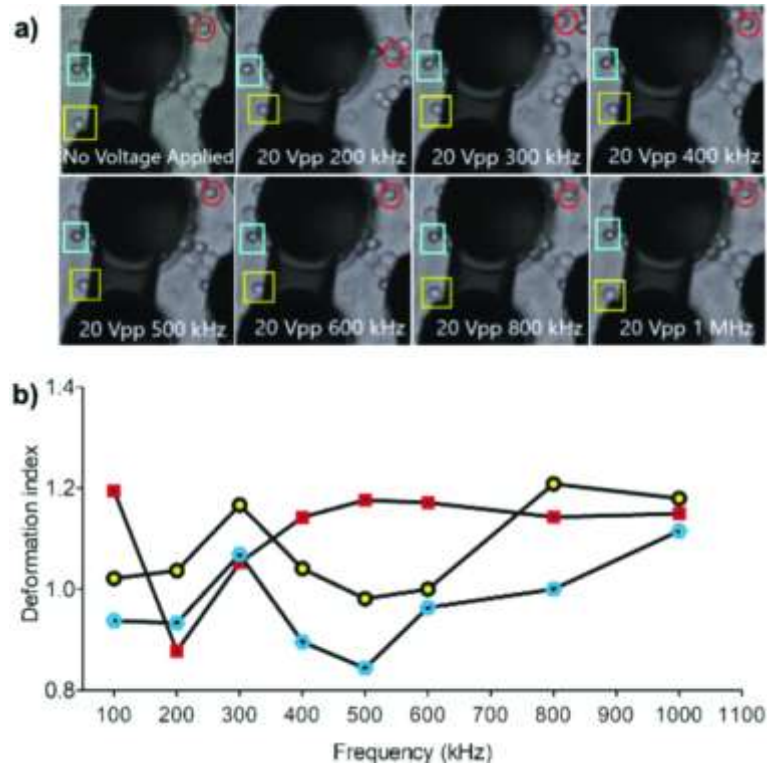


Figure 5.5.3: DEP deformation trends of three single monocytes. a) Behavior of three monocyte cells, indicated with red circle, blue rectangle and yellow square under the influences of increasing frequencies (20 Vpp, 0.2 – 1 MHz). b) The changes in the deformation indexes of the monocytes were color coded with red, blue and yellow to match with the cells in the images of a).

Dielectrophoretic forces were distributed the cells in the electrode array according to their polarizability difference, DEP forces were also capable of creating deformation on the cells. As mentioned above, monocytes and macrophages are well-known cells for their plastic properties [20,34]. When mammalian cells were exposed to large external flow forces in variable microenvironments using microfluidics, they became elongated, varied in size, and tended to return to their original shape once the external forces were removed [81,82].

We determined the dielectrophoretic deformation indexes (DDI) of the U937 monocytes and the U937-differentiated macrophages using the non-uniform AC electric field varying from 50 kHz to 1 MHz frequency. The DDI values of each monocyte and macrophage cells were calculated for 50 cells as defined in Eq.5 [106], where H (μm) was the height and W (μm) was the width of the cells.

$$DI = \frac{H}{W} \quad (5)$$

Fig. 5.5.4 illustrated the DDI distribution for the monocytes as population (Fig. 5.5.4.b) and at single cell sensitivity (Fig. 5.5.4.d) and macrophages as population (Fig. 5.5.4.c) and at single cell sensitivity (Fig. 5.5.4.e) including the outliers.

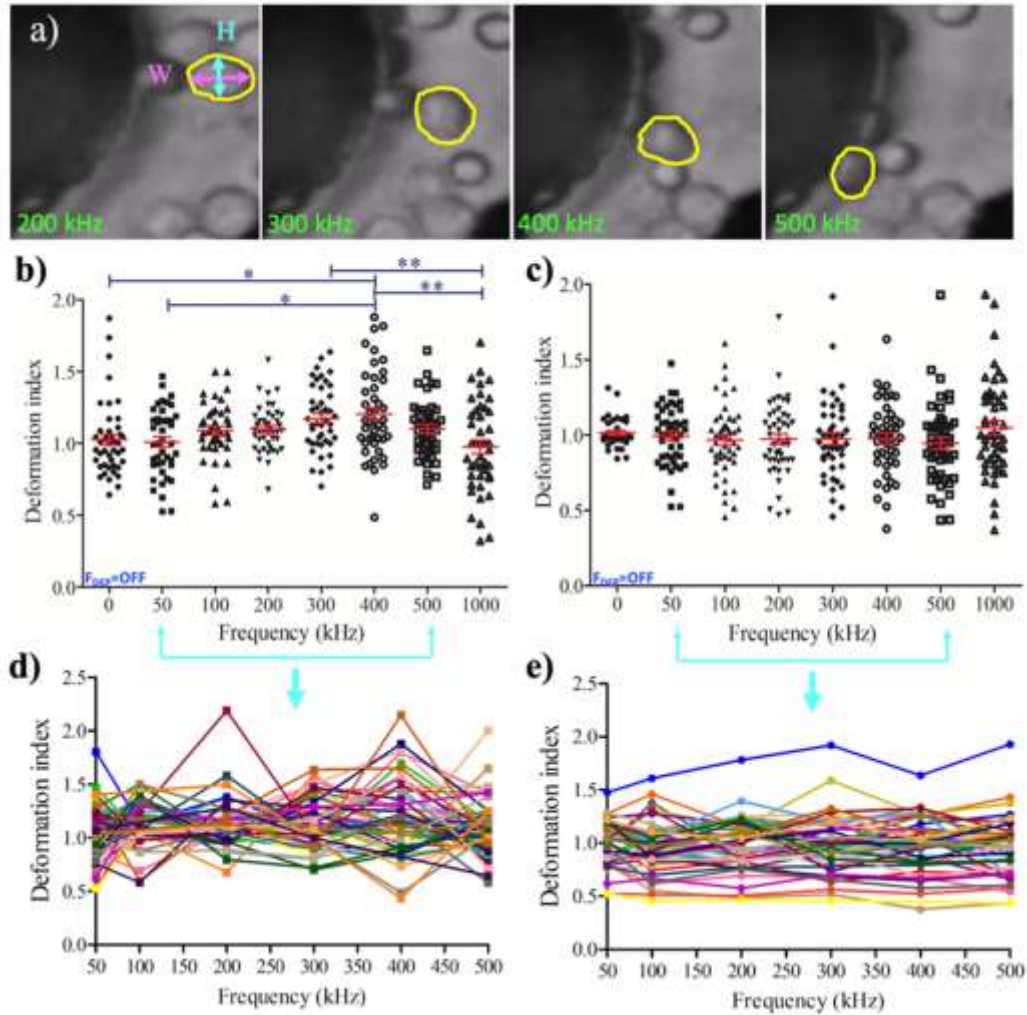


Figure 5.5.4: Dielectrophoretic deformation indexes (DDI) of U937 monocytes and U937-differentiated macrophages: (a) Representative image for the measurement of DDI. DDI values were presented with mean and standard error for population ($n = 45$). (b) single ($n = 47$) (d) monocyte cells; 45 population (c), single ($n = 47$) (e) macrophage cells. Tukey's multiple comparison test is applied for (b). * and ** indicate that data are significantly different with $p < 0.5$ and $p < 0.05$, respectively. Each color displays the change of

deformation indexes of single cells during the frequencies applied for the range of 50–500 kHz in (d) and (e).

Fig. 5.5.6 demonstrates that there was a significant DDI difference between U937 monocytes and U937-differentiated macrophages ($p < 0.05$) according to Tukey's Multiple Comparison Test.

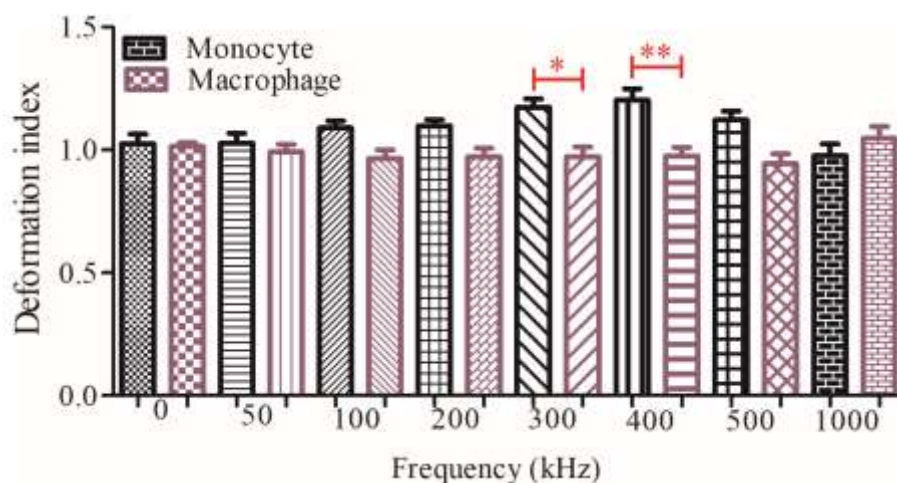


Figure 5.5.6: Comparison of the dielectrophoretic deformation indexes for the monocytes and macrophages without outliers. Measurements are the dielectrophoretic deformation index with mean and standard error for 45 monocyte and 45 macrophages cells. Tukey's multiple comparison test is applied. * and ** indicate that data are significantly different with $p < 0.5$ and $p < 0.05$, respectively.

6 CHAPTER SIX: DISCUSSION

6.1 Characterization of Heterogeneity in Microfabricated Tools

We demonstrate the phenotype of Glioblastoma cell line U87 in an unbiased, label free manner based on their adhesion, mobility, deformation propensities through the use of an engineered, microfluidic based platform. Using continuous monitoring for cell-cell adhesive properties (interacting) and deformation and motility changes (non-interacting) allowed single cell phenotypic analysis under well-defined conditions. In Fig.5.1. b and d, representative images of U87 and U87-C cultured on tissue culture-treated polystyrene (TPSC) surface shown on the upper side and cells cultured in PDMS microfluidic chip is shown bottom side as ordered. In Fig.5.1.a, the number of U87 and U87-C cells seeded in 12-well plates was counted using a hemocytometer at 24-hours intervals. The unpaired Student's t-test was performed and there was no significant growth difference found between the two groups during long-term conventional cell culture. In Fig.5.1.c, the number of U87 and U87-C cells in PDMS microfluidic chip at 12-hours intervals are given by counting cell numbers in microchambers by using ImageJ software.

Interestingly, instead of conventional methods, macrophage conditioned medium resulted with lower cellular growth with U87-C in the microchambers compared to U87. These results imply that the responses of brain cancer cells influenced under different maintenance factors can be quite complex and diverse [109,110]. To assess this diversity further, we performed wound healing assay and determined the migration ability of U87 and U87-C, representative phase images of U87 treated with DMEM (left panel) and U87-C cells treated with 50% DMEM and 50% conditioned media (right panel) after wound created, Fig.5.2. Images acquired with 10x magnification.

Measuring the U87-C wound area over time when comparing to U87 revealed specific migration changes and showed less impaired migratory phenotype. We observed that all macrophage conditioned stimulation caused very small decreases in the displacement of U87-C on TPSC surface compared to normal growth medium (Fig. 4.2.g).

Moreover, single cell lamellipodium formation, tail retraction, and directional movement may give an extra clue about migratory behaviors [111]. However, *in vivo*, cell movement is

much more heterogeneous than anticipated in 2D as the cells surrounded by extracellular matrix (ECM) and other cells [112]. Specially designed microchambers in microdevices serve as useful tools to examine how the cancer cells interact and conditioned maintenance factors modulates behavior [113].

A step further assessment is to observe individual cell's characteristics during migration. We measured the position of individual cells in microchambers. To minimize the influence of potential variabilities that may arise from differences of adherence time, elongation and shape differences when cells have first introduced the system; we performed measurements at the end of 48 hours upon cell loading. To further standardize the analysis, we used the same edge point of the same rectangular shape in the microchamber every 12 hours (Fig.3.2.1). The positions are assessed by following the center of the same cell and measuring its location.

In our results, the “x” position of U87 cells ranged around 500- μm while U87-C cells were -400 to -200- μm ; the “y” position of U87 cells range between 1000 and 1200- μm while U87-C cells were 0 to 400- μm . Speeds of U87-C cell population (n=20) found to be faster as a result of conditioned media stimulation compared to U-87 cells (n=20) in microchambers (Fig.3.2.1).

Cell size is determined from single cell deformation values. The channels of the microfluidic chip have rectangular dimensions of 1280 μm x 500 μm x 50 μm does not have any inducing shear effect to deform cells. Once cells introduced to microfluidic chips, they started to adhere and adapt to the surface with an extracellular organization and enabled us to analyze their steady-state deformability trends. Following that, they start to show their unique mechanical phenotype in response to environmental changes. The deformability of U87 cells was 2.2 times greater than U87-C cells, Fig.5.3.

To facilitate the comparison of measured single cell deformability, we introduced accumulative deformability and performed One-way analysis of variance, Tukey's Multiple Comparison test was carried out using GraphPad Prism (Version 5.0) software. The results were statistically significant at each interval ($p < 0.005$).

We demonstrate microfluidic platforms can show better understanding of the complex process of cancer metastasis and the utility of this system in the interrogation of phenotypic attributes associated with conditioned maintenance.

Using microfluidic platforms to assess mechanophenotypic properties of adhesive cells has important advantages. The cells can migrate along the microfluidic channel and the migration velocity can be tracked without losing spatial information. The optical transparency, gas permeability, low nutrition requirement, easy manipulation, being able to give high throughput results at a single-cell level have significant advantages compared to traditional migration assays. Utilizing microscale tools to give an adequate measurement of heterogeneous cell properties needed to elucidate disease mechanisms [114,115].

We used a specially constructed microfluidic design to allow cells to adhere and migrate along the channel [104]. In figure 3.2.1, the gap length was reduced between pillars with the help of rectangular-shaped ones and cells could move by adhering to a circle-shaped area [116]. Pillars helped to assign reference points to give consistent migration velocity resulting in varying intervals. We assigned the low right edge of the first rectangular pillar as a reference coordinate and calculated the migrated distance of cells at 12 hours intervals. The origin of the cell is pointed to as the curve area centroid of the cells, therefore, there was no misleading effect of neither image acquisition nor manual image analysis. We showed U87 cells as two populations: U87 glioma cells with the standard nutritional condition and U87-C glioma cells maintained in a conditional medium composed of standard and macrophage depleted medium with a ratio of 50%. Since we give mechanobiological parameters such as cell velocity, a conditional group was important to control to assess whether diminished and stressed maintenance conditions influence the migration potential of cells. Previously, U87-C growth was investigated in literature, and very similar growth was shown without any significant difference [104].

We quantified the velocity by single-cell tracking and measured it for both U87 and U87-C from 60 to 120 hours. In figure 5.4.1, while yellow labelled U87 cells showed uniform velocity change in both X- and Y-axis, blue and red labelled U87 cells showed increased velocity change between 84 and 120 hours. Next, we examined U87 and U87-C glioma cells' velocity change in X-axis and Y-axis, in Figure 5.4.2.a. U87 glioma cells velocity change in 12 hours was maximum $\sim 8 \mu\text{m}$ to -X-direction while maximum velocity change of another U87 cell was $\sim 6 \mu\text{m}$ to -Y direction (Fig.5.4.2.b). U87-C cells showed a slightly longer change compared to U87 (Fig.5.4.2.c and d). U87-C glioma cells showed a maximum $\sim 15 \mu\text{m}$ change in 12 hours along the X-axis and $\sim 114 \mu\text{m}$ along Y-axis to the positive direction.

These results confirmed the high heterogeneity, velocity, and migration potential of GBM [117,118]. We also showed the average velocity change of U87 and U87-C glioma cells in all time intervals (Fig. 5.4.3). The U87 and U87-C average velocities on X-axis were significantly different ($p=0,0012$) while the velocities on Y-axis did not show any significance. Our results indicate the glioma cells under extenuated culture conditions have slightly higher migration velocity compared to normal culture conditions.

Kolli-Bouhafs et al assessed the effect of Thymoquinone in astrocyte and glioma cells and they reported the migration speed of U87 as 8.55 ± 0.29 $\mu\text{m/h}$ in a fibronectin-treated petri dish, the migration speed was obtained by dividing the distance covered the scratch in 24 hours [119]. Li et al, quantified the velocity of C6 glioma cells in the time-lapse experiments with average cosine θ of 0.16 ± 0.02 for U87, 0.25 ± 0.03 for C6, and 0.17 ± 0.02 for U251 glioma cell lines to assess superoxide mediated directional migration. They used direct current (DC) electric fields with field strengths of 100, 200, 300, and 250 mV/mm in electrotactic chambers [86].

Sheykzadeh et al investigated the transferrin-conjugated porous silicon nanoparticles effect on GBM cell migration using microfluidic-based migration chip and they reported that the U87 cell migration was initiated by sending leading front cell protrusion across the microchannel [120]

The migration speed of rat C6 and patient-derived glioma cell bodies reported by Monzo et al was around 50 $\mu\text{m/h}$ on laminin-coated micropatterned linear tracks while Sheykzadeh et al reported the U87 cell migration 10 $\mu\text{m/h}$ [121]. Prah et al reported the malignant glioblastoma cell line, U251, migration speed as 30 $\mu\text{m/h}$ in 12 μm x 5 μm linear channel [122].

The dispersal velocity of U87, LN-229, and U118-MG cell line aggregates reported 21.4 ± 2.9 $\mu\text{m/h}$, 4.9 ± 0.6 $\mu\text{m/h}$, and 4.1 ± 0.6 $\mu\text{m/h}$ on a solid substrate, respectively [123]. Kiss et al reported the velocity of U87 cell line as 50 ± 30 $\mu\text{m/h}$ by measuring displacement of cell nuclei on phase contrast images for 14 hours [124]. The U87 cells, cultured in different stiffness regions under epidermal growth factor stimulation, speed was reported as ~ 40 $\mu\text{m/h}$ on the stiff end but ~ 20 $\mu\text{m/h}$ on the soft end [125]. In the migration assay developed by Irimia and Toner, different types of cancer cells velocities reported for 24-48 hours long [126]. They used two different cancer drugs to assess migration reduction and reported the

U87 speed as $36.4 \pm 2.5 \mu\text{m/h}$. Since the time interval that we analyzed the migration velocity of glioma cells is the longest time interval reported to the best of our knowledge, we believe that the differences may be due to time. Also, the microchannels we used here had a larger area, this difference may be due to the level of confinement.

To our knowledge, our study is the first demonstration that gives glioblastoma cell velocity in longest culture time (120 hours) and at single cell sensitivity. There are several drawbacks in reference studies such as employment of glycoproteins that can bind extracellular matrices, bulk measurement of large numbers of cells in wound area or usage of very thin channels that may lead cell elongation and they lack nutritional assessment in varying conditions. All these results taken together, glioma cells culture condition affects morphology, displacement, velocity, and migratory behavior.

GBM cell lines velocity requires comprehensive assessment from fresh isolates of brain tumor cell lines or human brain samples. The link between velocity and metastatic parameters should be assessed to evaluate this result into clinical applications. We believe that measuring migration velocity in our microfluidic platform could be used to assess therapeutic agents or as a method to evaluate the molecular determinants underlying the heterogeneity mechanisms, all of which are critical for improving clinical outcomes.

Lab-on-chip methods can determine mechanical differences of invasive cancers, Remmerbach et al. carried mechanical phenotyping of primary tumor cells ($n \approx 30$ cells) from histopathologically confirmed patient samples to screen cancer using microfluidic optical stretcher, oral cancer cells were on average 3.5 times more deformable than normal oral epithelial cells [127].

The direct comparison presented in single cell deformability provides context for the interpretation of behavioral change measurements performed with high throughput. Besides, the migration assay done on TPSC surfaces showed minimal correlation and were statistically not significant. These varying changes urged us to investigate Epithelial to Mesenchymal Transition (EMT), which causes epithelial cells to lose their characteristics and gain mesenchymal phenotypic especially in high heterogenetic and invasive cancer types such as GBM [128].

Cancer cells lose their cell-cell junctions and fibroblast-like invasiveness during EMT [129]. In GBM, cells lose their adhesion molecules which are crucial for tight junctions, and

apical basal polarity [130,131]. Stressed maintenance conditions, such as serum starvation and conditioned media, may result with EMT in terms of being promoted via complex signaling networks, tyrosine kinase receptors, growth factors and ECM components [30,132]. EMT is critical for stem cell formation, wound healing and cancer progression [27].

Shiube and Weinberg have shown that epithelial cell marker E-cadherin has been downregulated whereas mesenchymal markers such as N-cadherin, Vimentin are upregulated during EMT [130].

To investigate the extracellular change that may be a result of EMT caused by maintenance conditions, cells were stained with the specific antibodies against E-cadherin and Vimentin. Results obtained so far showed that mechanical phenotyping of GBM cells can identify the differences that conventional methods cannot. The E-Cadherin level of U87 was increased while the U87-C level was decreasing (Fig.4.4.1). The Vimentin level of U87 was increased while the U87-C level was decreasing (Fig.4.4.2). Both protein expressions tend to increase dynamically for the U87 while U-87-C protein levels ramped down.

7 CHAPTER SEVEN: CONCLUSIONS

7.1 Conclusion

Monocytes and macrophage cells, derived from the same monocyte cells, have been compared according to their dielectrophoretic mobility and deformation. Both monocyte and macrophage populations exhibited inter-individual differences due to their intrinsic properties such as size, shape, changes in membrane surface organization that may result in heterogeneity in their DEP responses.

Incorporating mechanical phenotyping methods into the existing knowledge of cellular properties opens the way toward a broader understanding of physiological processes and gives greater assistance of clinical diagnostic methods. Validations and demonstrations of methods to assess mechanical cell properties are great motivations for new developments.

This variability of single cell properties within the same population is mostly attributed to the differences between shear forces, stress factors, laminar effects, cell preparations etc. Here, we complemented this analysis by only changing one variable in maintenance condition and presented a mechanical phenotyping comparison of two types of commonly used techniques. In contrast to different microfluidic cell deformability analysis, we did not perform any additional strain rates and stresses, and we used steady long-term cell culture instead of using short term cell suspension which reduces potential sources of variability.

Microfluidic lab-on-a-chip devices enable phenotyping of individual cells with controlled gradients and well-defined shapes enabling them to receive extensive high-throughput. Our study presents important clues about GBM cells phenotype and may be useful to develop recent advances in diagnosis and improve therapeutic strategies to immunotherapy, as the current progress in identifying efficient therapies to support the survival is yet to result in substantial clinical benefit. We suggest that the EMT of Glioblastoma should be further interrogated using microfluidic platforms to help clinical studies.

Experiments in the microfluidic device and cell culture dishes confirmed high heterogeneity in glioma and macrophage populations. In the conditional culture of glioma cells obtained from macrophages, the proliferation rate slowed down, and the migration rate increased. When glioma cells were cultured with macrophages, the proliferation rate slowed

down, a decrease in the number of spheroids they formed and an increase in the area covered by the spheroids were measured. Expression of Vimentin protein was increased in the center of spheroids, whereas E-cadherin did not change. It has been confirmed that macrophages within spheroids acquire M2 phenotypic features.

In light of our results, the single cell microfluidic analysis provides a better understanding of basal and mechanical changes in the short-term period. Our results show a method for studies in high heterogenetic cancers of interest.

7.2 Future research directions

The complex, dynamic and highly heterogeneous microenvironment of glioblastoma tumors is poorly understood using conventional macroscale techniques, we need to develop new methods and tools to explore the important and measurable properties of these cells. In order to elucidate the mechanisms underlying the heterogeneity of the tumor microenvironment, it is necessary to measure cellular properties at the single cell level for many cell populations and to compile the results with available data in the literature. However, an unfilled gap still exists between the understanding of the different cell types and proteins achievable with well-established, macro-scale assay types and micro-scale analysis. Standardized and well-established lab-on-chip analysis techniques needed.

Our further studies will focus on separation and recovery of cells with different deformation indexes from the 3D-carbon DEP platform for downstream analysis using immunostaining and quantitative reverse transcription-polymerase chain reaction (RT-qPCR) techniques. Hence, we can promptly explain the dielectrophoretic mobility and deformation differences in terms of transcription and protein expression levels in the membrane surface and cytoskeletal components. Moreover, we can employ this method for further characterization of macrophage subpopulations, it may provide value in increasing our understanding of the nature of TAMs.

BIBLIOGRAPHY

- [1] M. Urbanska, H.E. Muñoz, J. Shaw Bagnall, O. Otto, S.R. Manalis, D. Di Carlo, J. Guck, A comparison of microfluidic methods for high-throughput cell deformability measurements, *Nat. Methods.* 17 (2020) 587–593. <https://doi.org/10.1038/s41592-020-0818-8>.
- [2] P.O. Krutzik, G.P. Nolan, Fluorescent cell barcoding in flow cytometry allows high-throughput drug screening and signaling profiling, *Nat. Methods.* 3 (2006) 361–368. <https://doi.org/10.1038/nmeth872>.
- [3] M. Radmacher, Studying the Mechanics of Cellular Processes by Atomic Force Microscopy, *Methods Cell Biol.* 83 (2007) 347–372. [https://doi.org/10.1016/S0091-679X\(07\)83015-9](https://doi.org/10.1016/S0091-679X(07)83015-9).
- [4] J. Guck, R. Ananthkrishnan, H. Mahmood, T.J. Moon, C.C. Cunningham, J. Käs, The optical stretcher: A novel laser tool to micromanipulate cells, *Biophys. J.* 81 (2001) 767–784. [https://doi.org/10.1016/S0006-3495\(01\)75740-2](https://doi.org/10.1016/S0006-3495(01)75740-2).
- [5] M. Musielak, Red blood cell-deformability measurement: Review of techniques, *Clin. Hemorheol. Microcirc.* 42 (2009) 47–64. <https://doi.org/10.3233/CH-2009-1187>.
- [6] M. Elitas, R. Martinez-Duarte, N. Dhar, J.D. McKinney, P. Renaud, Dielectrophoresis-based purification of antibiotic-treated bacterial subpopulations, *Lab Chip.* 14 (2014) 1850–1857. <https://doi.org/10.1039/c4lc00109e>.
- [7] J. Gienger, H. Gross, V. Ost, M. Bär, J. Neukammer, Assessment of deformation of human red blood cells in flow cytometry: measurement and simulation of bimodal forward scatter distributions, *Biomed. Opt. Express.* 10 (2019) 4531. <https://doi.org/10.1364/boe.10.004531>.
- [8] H. Harrison, X. Lu, S. Patel, C. Thomas, A. Todd, M. Johnson, Y. Raval, T.R. Tzeng, Y. Song, J. Wang, D. Li, X. Xuan, Electrokinetic preconcentration of particles and cells in microfluidic reservoirs, *Analyst.* 140 (2015) 2869–2875. <https://doi.org/10.1039/c5an00105f>.
- [9] J.H. Moore, C. Honrado, V. Stagnaro, G. Kolling, C.A. Warren, N.S. Swami, Rapid in Vitro Assessment of *Clostridioides difficile* Inhibition by Probiotics Using Dielectrophoresis to Quantify Cell Structure Alterations, *ACS Infect. Dis.* 6 (2020) 1000–1007. <https://doi.org/10.1021/acsinfecdis.9b00415>.
- [10] M.U. Ahmed, I. Saaem, P.C. Wu, A.S. Brown, Personalized diagnostics and biosensors: A review of the biology and technology needed for personalized medicine, *Crit. Rev. Biotechnol.* 34 (2014) 180–196. <https://doi.org/10.3109/07388551.2013.778228>.
- [11] E. Samiei, M. Tabrizian, M. Hoorfar, A review of digital microfluidics as portable platforms for lab-on a-chip applications, *Lab Chip.* 16 (2016) 2376–2396. <https://doi.org/10.1039/c6lc00387g>.
- [12] Q.T. Ostrom, L. Bauchet, F.G. Davis, I. Deltour, J.L. Fisher, C.E. Langer, M. Pekmezci, J.A. Schwartzbaum, M.C. Turner, K.M. Walsh, M.R. Wrensch, J.S. Barnholtz-Sloan, The epidemiology of glioma in adults: A state of the science review, *Neuro. Oncol.* 16 (2014) 896–913. <https://doi.org/10.1093/neuonc/nou087>.
- [13] T. Komori, The 2016 WHO classification of tumours of the central nervous system: The major points of revision, *Neurol. Med. Chir. (Tokyo).* 57 (2017) 301–311. <https://doi.org/10.2176/nmc.ra.2017-0010>.
- [14] M. Snuderl, L. Fazlollahi, L.P. Le, M. Nitta, B.H. Zhelyazkova, C.J. Davidson, S.

- Akhavanfard, D.P. Cahill, K.D. Aldape, R.A. Betensky, D.N. Louis, A.J. Iafrate, Mosaic amplification of multiple receptor tyrosine kinase genes in glioblastoma, *Cancer Cell*. 20 (2011) 810–817. <https://doi.org/10.1016/j.ccr.2011.11.005>.
- [15] G.C. Nickel, J. Barnholtz-Sloan, M.P. Gould, S. McMahon, A. Cohen, M.D. Adams, K. Guda, M. Cohen, A.E. Sloan, T. LaFramboise, Characterizing mutational heterogeneity in a glioblastoma patient with double recurrence, *PLoS One*. 7 (2012) e35262. <https://doi.org/10.1371/journal.pone.0035262>.
- [16] N.J. Szerlip, A. Pedraza, D. Chakravarty, M. Azim, J. McGuire, Y. Fang, T. Ozawa, E.C. Holland, J.T. Hused, S. Jhanwar, M.A. Leversha, T. Mikkelsen, C.W. Brennan, Intratumoral heterogeneity of receptor tyrosine kinases EGFR and PDGFRA amplification in glioblastoma defines subpopulations with distinct growth factor response, *Proc. Natl. Acad. Sci. U. S. A.* 109 (2012) 3041–3046. <https://doi.org/10.1073/pnas.1114033109>.
- [17] O.J. Becher, D. Hambardzumyan, E.I. Fomchenko, H. Momota, L. Mainwaring, A.M. Bleau, A.M. Katz, M. Edgar, A.M. Kenney, C. Cordon-Cardo, R.G. Blasberg, E.C. Holland, Gli activity correlates with tumor grade in platelet-derived growth factor-induced gliomas, *Cancer Res*. 68 (2008) 2241–2249. <https://doi.org/10.1158/0008-5472.CAN-07-6350>.
- [18] N.A. Charles, E.C. Holland, R. Gilbertson, R. Glass, H. Kettenmann, The brain tumor microenvironment, *Glia*. 60 (2012) 502–514. <https://doi.org/10.1002/glia.21264>.
- [19] S. DeCordova, A. Shastri, A.G. Tsolaki, H. Yasmin, L. Klein, S.K. Singh, U. Kishore, Molecular Heterogeneity and Immunosuppressive Microenvironment in Glioblastoma, *Front. Immunol.* 11 (2020) 1402. <https://doi.org/10.3389/fimmu.2020.01402>.
- [20] Brenton D. Hoffman; John C. Crocker, Cell Mechanics: Dissecting the Physical Responses of Cells to Force, *Annu. Rev. Biomed. Eng.* 11 (2009) 259–288. <https://doi.org/10.1146/annurev.bioeng.10.061807.160511>.
- [21] Cancer heterogeneity: implications for targeted therapeutics | *British Journal of Cancer*, (n.d.). <https://www.nature.com/articles/bjc2012581> (accessed May 8, 2021).
- [22] Q.W. Fan, C.K. Cheng, W.C. Gustafson, E. Charron, P. Zipper, R.A. Wong, J. Chen, J. Lau, C. Knobbe-Thomsen, M. Weller, N. Jura, G. Reifenberger, K.M. Shokat, W.A. Weiss, EGFR Phosphorylates Tumor-Derived EGFRvIII Driving STAT3/5 and Progression in Glioblastoma, *Cancer Cell*. 24 (2013) 438–449. <https://doi.org/10.1016/j.ccr.2013.09.004>.
- [23] R.C. Gimple, S. Bhargava, D. Dixit, J.N. Rich, Glioblastoma stem cells: Lessons from the tumor hierarchy in a lethal cancer, *Genes Dev*. 33 (2019) 591–609. <https://doi.org/10.1101/gad.324301.119>.
- [24] S. Caragher, A.J. Chalmers, N. Gomez-Roman, Glioblastoma’s next top model: Novel culture systems for brain cancer radiotherapy research, *Cancers (Basel)*. 11 (2019). <https://doi.org/10.3390/cancers11010044>.
- [25] Y. Takashima, A. Kawaguchi, R. Yamanaka, Promising Prognosis Marker Candidates on the Status of Epithelial-Mesenchymal Transition and Glioma Stem Cells in Glioblastoma, *Cells*. 8 (2019). <https://doi.org/10.3390/cells8111312>.
- [26] Y. Iwadate, Epithelial-mesenchymal transition in glioblastoma progression, *Oncol. Lett*. 11 (2016) 1615–1620. <https://doi.org/10.3892/ol.2016.4113>.
- [27] A. Kuşoğlu, Ç. Biray Avcı, Cancer stem cells: A brief review of the current status, *Gene*. 681 (2019) 80–85. <https://doi.org/10.1016/j.gene.2018.09.052>.

- [28] Q. Chi, H. Xu, D. Song, Z. Wang, Z. Wang, G. Ma, α -E-Catenin (CTNNA1) inhibits cell proliferation, invasion and EMT of bladder cancer, *Cancer Manag. Res.* 12 (2020) 12747–12758. <https://doi.org/10.2147/CMAR.S259269>.
- [29] and C.B. Heidi Phillips, Thomas Sandmann, Congfen Li, Timothy Francis Cloughesy, Olivier L. Chinot, Wolfgang Wick, Ryo Nishikawa, Warren P. Mason, Roger Henriksson, Frank Saran, Albert Lai, Nicola Moore, Priti S. Hegde, Lauren E. Abrey, Richard Bourgon, Josep Garc, Correlation of molecular subtypes with survival in AVAglio (bevacizumab [Bv] and radiotherapy [RT] and temozolomide [T] for newly diagnosed glioblastoma [GB]), *J. Clin. Oncol.* 32 (2014).
- [30] H. Acloque, M.S. Adams, K. Fishwick, M. Bronner-Fraser, M.A. Nieto, Epithelial-mesenchymal transitions: The importance of changing cell state in development and disease, *J. Clin. Invest.* 119 (2009) 1438–1449. <https://doi.org/10.1172/JCI38019>.
- [31] H. Peinado, D. Olmeda, A. Cano, Snail, ZEB and bHLH factors in tumour progression: An alliance against the epithelial phenotype?, *Nat. Rev. Cancer.* 7 (2007) 415–428. <https://doi.org/10.1038/nrc2131>.
- [32] M. Ghorbani, G. Alcan, M. Unel, D. Gozuacik, S. Ekici, H. Uvet, A. Sabanovic, A. Kosar, Visualization of microscale cavitating flow regimes via particle shadow sizing imaging and vision based estimation of the cone angle, *Exp. Therm. Fluid Sci.* 78 (2016) 322–333. <https://doi.org/https://doi.org/10.1016/j.expthermflusci.2016.04.026>.
- [33] A. Francou, K. V. Anderson, The Epithelial-to-Mesenchymal Transition in Development and Cancer, *Annu. Rev. Cancer Biol.* 4 (2020) 197–220. <https://doi.org/10.1146/annurev-cancerbio-030518-055425>.
- [34] A. Chauviere, L. Preziosi, H. Byrne, A model of cell migration within the extracellular matrix based on a phenotypic switching mechanism, *Math. Med. Biol.* 27 (2009) 255–281. <https://doi.org/10.1093/imammb/dqp021>.
- [35] P.R. Taylor, S. Gordon, Monocyte heterogeneity and innate immunity, *Immunity.* 19 (2003) 2–4. [https://doi.org/10.1016/S1074-7613\(03\)00178-X](https://doi.org/10.1016/S1074-7613(03)00178-X).
- [36] D.A. Hume, K.P.A. MacDonald, Therapeutic applications of macrophage colony-stimulating factor-1 (CSF-1) and antagonists of CSF-1 receptor (CSF-1R) signaling, *Blood.* 119 (2012) 1810–1820. <https://doi.org/10.1182/blood-2011-09-379214>.
- [37] S. Gordon, Alternative activation of macrophages, *Nat. Rev. Immunol.* 3 (2003) 23–35. <https://doi.org/10.1038/nri978>.
- [38] J.P. Edwards, X. Zhang, K.A. Frauwirth, D.M. Mosser, Biochemical and functional characterization of three activated macrophage populations, *J. Leukoc. Biol.* 80 (2006) 1298–1307. <https://doi.org/10.1189/jlb.0406249>.
- [39] D.M. Mosser, J.P. Edwards, Exploring the full spectrum of macrophage activation, *Nat. Rev. Immunol.* 8 (2008) 958–969. <https://doi.org/10.1038/nri2448>.
- [40] M.R. Galdiero, C. Garlanda, S. Jaillon, G. Marone, A. Mantovani, Tumor associated macrophages and neutrophils in tumor progression, *J. Cell. Physiol.* 228 (2013) 1404–1412. <https://doi.org/10.1002/jcp.24260>.
- [41] D. Grishenkov, C. Pecorari, T.B. Brismar, G. Paradossi, Characterization of Acoustic Properties of PVA-Shelled Ultrasound Contrast Agents: Linear Properties (Part I), *Ultrasound Med. Biol.* 35 (2009) 1127–1138. <https://doi.org/https://doi.org/10.1016/j.ultrasmedbio.2009.02.002>.
- [42] C. Atri, F.Z. Guerfali, D. Laouini, Role of human macrophage polarization in inflammation during infectious diseases, *Int. J. Mol. Sci.* 19 (2018).

- <https://doi.org/10.3390/ijms19061801>.
- [43] M. Zhang, G. Hutter, S.A. Kahn, T.D. Azad, S. Gholamin, C.Y. Xu, J. Liu, A.S. Achrol, C. Richard, P. Sommerkamp, M.K. Schoen, M.N. McCracken, R. Majeti, I. Weissman, S.S. Mitra, S.H. Cheshier, Anti-CD47 treatment stimulates phagocytosis of glioblastoma by M1 and M2 polarized macrophages and promotes M1 polarized macrophages in vivo, *PLoS One*. 11 (2016) 1–21. <https://doi.org/10.1371/journal.pone.0153550>.
- [44] K.Y. Lee, M1 and M2 polarization of macrophages: a mini-review, *Med. Biol. Sci. Eng.* 2 (2019) 1–5. <https://doi.org/10.30579/mbse.2019.2.1.1>.
- [45] L. Tao, G. Huang, H. Song, Y. Chen, L. Chen, Cancer associated fibroblasts: An essential role in the tumor microenvironment (review), *Oncol. Lett.* 14 (2017) 2611–2620. <https://doi.org/10.3892/ol.2017.6497>.
- [46] F. Balkwill, K.A. Charles, A. Mantovani, Smoldering and polarized inflammation in the initiation and promotion of malignant disease, *Cancer Cell*. 7 (2005) 211–217. <https://doi.org/10.1016/j.ccr.2005.02.013>.
- [47] L.M. Coussens, Z. Werb, Inflammatory cells and cancer: Think different!, *J. Exp. Med.* 193 (2001) 6–9. <https://doi.org/10.1084/jem.193.6.F23>.
- [48] I. Tabas, A.H. Lichtman, Monocyte-Macrophages and T Cells in Atherosclerosis, *Immunity*. 47 (2017) 621–634. <https://doi.org/10.1016/j.immuni.2017.09.008>.
- [49] M.J. Pittet, F.K. Swirski, Monocytes link atherosclerosis and cancer, *Eur. J. Immunol.* 41 (2011) 2519–2522. <https://doi.org/10.1002/eji.201141727>.
- [50] A. Etzerodt, K. Tsalkitzi, M. Maniecki, W. Damsky, M. Delfini, E. Baudoin, M. Moulin, M. Bosenberg, J.H. Graversen, N. Auphan-Anezin, S.K. Moestrup, T. Lawrence, Specific targeting of CD163+ TAMs mobilizes inflammatory monocytes and promotes T cell-mediated tumor regression, *J. Exp. Med.* 216 (2019) 2394–2411. <https://doi.org/10.1084/jem.20182124>.
- [51] J.D. Thiriou, Y.B. Martinez-Martinez, J.J. Endsley, A.G. Torres, Hacking the host: Exploitation of macrophage polarization by intracellular bacterial pathogens, *Pathog. Dis.* 78 (2020) 1–14. <https://doi.org/10.1093/FEMSPD/FTAA009>.
- [52] S.A. Eming, T. Krieg, J.M. Davidson, Inflammation in wound repair: Molecular and cellular mechanisms, *J. Invest. Dermatol.* 127 (2007) 514–525. <https://doi.org/10.1038/sj.jid.5700701>.
- [53] P.A. Muller, B. Koscsó, G.M. Rajani, K. Stevanovic, M.L. Berres, D. Hashimoto, A. Mortha, M. Leboeuf, X.M. Li, D. Mucida, E.R. Stanley, S. Dahan, K.G. Margolis, M.D. Gershon, M. Merad, M. Bogunovic, Crosstalk between muscularis macrophages and enteric neurons regulates gastrointestinal motility, *Cell*. 158 (2014) 300–313. <https://doi.org/10.1016/j.cell.2014.04.050>.
- [54] T.A. Wynn, A. Chawla, J.W. Pollard, Macrophage biology in development, homeostasis and disease, *Nature*. 496 (2013) 445–455. <https://doi.org/10.1038/nature12034>.
- [55] S. Epelman, K.J. Lavine, G.J. Randolph, Origin and Functions of Tissue Macrophages, *Immunity*. 41 (2014) 21–35. <https://doi.org/10.1016/j.immuni.2014.06.013>.
- [56] Y. Okabe, R. Medzhitov, Tissue-specific signals control reversible program of localization and functional polarization of macrophages, *Cell*. 157 (2014) 832–844. <https://doi.org/10.1016/j.cell.2014.04.016>.
- [57] J. Xue, S. V. Schmidt, J. Sander, A. Draffehn, W. Krebs, I. Quester, D. DeNardo, T.D. Gohel, M. Emde, L. Schmidleithner, H. Ganesan, A. Nino-Castro, M.R. Mallmann, L.

- Labzin, H. Theis, M. Kraut, M. Beyer, E. Latz, T.C. Freeman, T. Ulas, J.L. Schultze, Transcriptome-Based Network Analysis Reveals a Spectrum Model of Human Macrophage Activation, *Immunity*. 40 (2014) 274–288. <https://doi.org/10.1016/j.immuni.2014.01.006>.
- [58] D. Di Carlo, A mechanical biomarker of cell state in medicine, *J. Lab. Autom.* 17 (2012) 32–42. <https://doi.org/10.1177/2211068211431630>.
- [59] J. Folkman, A. Moscona, Role of cell shape in growth control, *Nature*. 273 (1978) 345–349. <https://doi.org/10.1038/273345a0>.
- [60] J. Guck, S. Schinkinger, B. Lincoln, F. Wottawah, S. Ebert, M. Romeyke, D. Lenz, H.M. Erickson, R. Ananthakrishnan, D. Mitchell, J. Kas, S. Ulvick, C. Bilby, Optical deformability as an inherent cell marker for testing malignant transformation and metastatic competence, *Biophys. J.* 88 (2005) 3689–3698. <https://doi.org/10.1529/biophysj.104.045476>.
- [61] D.M. Thompson, K.R. King, K.J. Wieder, M. Toner, M.L. Yarmush, A. Jayaraman, Dynamic gene expression profiling using a microfabricated living cell array, *Anal. Chem.* 76 (2004) 4098–4103. <https://doi.org/10.1021/ac0354241>.
- [62] K.B. Riether, M.A. Dollard, P. Billard, Assessment of heavy metal bioavailability using *Escherichia coli* zntAp::lux and copAp::lux-based biosensors, *Appl. Microbiol. Biotechnol.* 57 (2001) 712–716. <https://doi.org/10.1007/s00253-001-0852-0>.
- [63] K. Turner, S. Xu, P. Pasini, S. Deo, L. Bachas, S. Daunert, Hydroxylated polychlorinated biphenyl detection based on a genetically engineered bioluminescent whole-cell sensing system, *Anal. Chem.* 79 (2007) 5740–5745. <https://doi.org/10.1021/ac0705162>.
- [64] M.A. Walling, J.R.E. Shepard, Cellular heterogeneity and live cell arrays, *Chem. Soc. Rev.* 40 (2011) 4049–4076. <https://doi.org/10.1039/c0cs00212g>.
- [65] R.M. Hochmuth, Micropipette aspiration of living cells, *J. Biomech.* 33 (2000) 15–22. [https://doi.org/10.1016/S0021-9290\(99\)00175-X](https://doi.org/10.1016/S0021-9290(99)00175-X).
- [66] O. Thoumine, A. Ott, O. Cardoso, J.J. Meister, Microplates: A new tool for manipulation and mechanical perturbation of individual cells, *J. Biochem. Biophys. Methods*. 39 (1999) 47–62. [https://doi.org/10.1016/S0165-022X\(98\)00052-9](https://doi.org/10.1016/S0165-022X(98)00052-9).
- [67] G. Artmann, A microscopic photometric method for measuring erythrocyte deformability. *Clinical Hemorheology and Microcirculation*, *Clin. Hemorheol. Microcirc.* 6 (1986) 617–627.
- [68] J.P. Nolan, L.A. Sklar, Sensitive , Real-Time Measurements of Molecular Interactions, (1998) 633–638.
- [69] G. Eluru, R. Srinivasan, S.S. Gorthi, Deformability Measurement of Single-Cells at High-Throughput With Imaging Flow Cytometry, *J. Light. Technol.* 33 (2015) 3475–3480. <https://doi.org/10.1109/JLT.2015.2413834>.
- [70] A.E. Pelling, F.S. Veraitch, C.P.K. Chu, C. Mason, M.A. Horton, Mechanical dynamics of single cells during early apoptosis, *Cell Motil. Cytoskeleton*. 66 (2009) 409–422. <https://doi.org/10.1002/cm.20391>.
- [71] C. Qian, H. Huang, L. Chen, X. Li, Z. Ge, T. Chen, Z. Yang, L. Sun, Dielectrophoresis for bioparticle manipulation, *Int. J. Mol. Sci.* 15 (2014) 18281–18309. <https://doi.org/10.3390/ijms151018281>.
- [72] Y. Zhao, D. Wang, T. Xu, P. Liu, Y. Cao, Y. Wang, X. Yang, X. Xu, X. Wang, H. Niu, Bladder cancer cells re-educate TAMs through lactate shuttling in the microfluidic cancer microenvironment, *Oncotarget*. 6 (2015) 39196–39210.

- <https://doi.org/10.18632/oncotarget.5538>.
- [73] P.H. Wu, D.R. Ben Aroush, A. Asnacios, W.C. Chen, M.E. Dokukin, B.L. Doss, P. Durand-Smet, A. Ekpenyong, J. Guck, N. V. Guz, P.A. Janmey, J.S.H. Lee, N.M. Moore, A. Ott, Y.C. Poh, R. Ros, M. Sander, I. Sokolov, J.R. Staunton, N. Wang, G. Whyte, D. Wirtz, A comparison of methods to assess cell mechanical properties, *Nat. Methods*. 15 (2018). <https://doi.org/10.1038/s41592-018-0015-1>.
- [74] M. Shin, Sehyun; Ku, Yun-Hee; Ho, Jian-Xun; Kim, Yu-Kyung; Suh, Jang-Soo; Singh, Progressive impairment of erythrocyte deformability as indicator of microangiopathy in type 2 diabetes mellitus, *Clin. Hemorheol. Microcirc.* 36 (2006) 253–261.
- [75] L.P. Di Carlo, Dino; Lee, -CELL ANALYSIS for Quantitative Biology, (n.d.).
- [76] E.S. Elvington, A. Salmanzadeh, M.A. Stremmer, R. V. Davalos, Label-free isolation and enrichment of cells through contactless dielectrophoresis, *J. Vis. Exp.* (2013) 1–10. <https://doi.org/10.3791/50634>.
- [77] P. Eaton, C.P. do Amaral, S.C.P. Couto, M.S. Oliveira, A.G. Vasconcelos, T.K.S. Borges, S.A.S. Kückelhaus, J.R.S.A. Leite, M.I. Muniz-Junqueira, Atomic Force Microscopy Is a Potent Technique to Study Eosinophil Activation, *Front. Physiol.* 10 (2019). <https://doi.org/10.3389/fphys.2019.01261>.
- [78] K.C. Neuman, A. Nagy, Single-molecule force spectroscopy: Optical tweezers, magnetic tweezers and atomic force microscopy, *Nat. Methods*. 5 (2008) 491–505. <https://doi.org/10.1038/nmeth.1218>.
- [79] R. Zhao, K.L. Sider, C.A. Simmons, Measurement of layer-specific mechanical properties in multilayered biomaterials by micropipette aspiration, *Acta Biomater.* 7 (2011) 1220–1227. <https://doi.org/10.1016/j.actbio.2010.11.004>.
- [80] G. Artmann, A microscopic photometric method for measuring erythrocyte deformability, *Clin. Hemorheol.* 6 (1986) 617–627. <https://doi.org/10.3233/ch-1986-6613>.
- [81] N.F. Zeng, J.E. Mancuso, A.M. Zivkovic, J.T. Smilowitz, W.D. Ristenpart, Red blood cells from individuals with abdominal obesity or metabolic abnormalities exhibit less deformability upon entering a constriction, *PLoS One*. 11 (2016) 1–12. <https://doi.org/10.1371/journal.pone.0156070>.
- [82] H. Liang, Y. Zhang, D. Chen, H. Tan, Y. Zheng, J. Wang, J. Chen, Characterization of single-nucleus electrical properties by microfluidic constriction channel, *Micromachines*. 10 (2019) 38–40. <https://doi.org/10.3390/mi10110740>.
- [83] X. Xu, Y. Hou, X. Yin, L. Bao, A. Tang, L. Song, F. Li, S. Tsang, K. Wu, H. Wu, W. He, L. Zeng, M. Xing, R. Wu, H. Jiang, X. Liu, D. Cao, G. Guo, X. Hu, Y. Gui, Z. Li, W. Xie, X. Sun, M. Shi, Z. Cai, B. Wang, M. Zhong, J. Li, Z. Lu, N. Gu, X. Zhang, L. Goodman, L. Bolund, J. Wang, H. Yang, K. Kristiansen, M. Dean, Y. Li, J. Wang, Single-cell exome sequencing reveals single-nucleotide mutation characteristics of a kidney tumor, *Cell*. 148 (2012) 886–895. <https://doi.org/10.1016/j.cell.2012.02.025>.
- [84] A. Shamloo, N. Ma, M.M. Poo, L.L. Sohn, S.C. Heilshorn, Endothelial cell polarization and chemotaxis in a microfluidic device, *Lab Chip*. 8 (2008) 1292–1299. <https://doi.org/10.1039/b719788h>.
- [85] E. Leclerc, Y. Sakai, T. Fujii, Microfluidic PDMS (Polydimethylsiloxane) bioreactor for large-scale culture of hepatocytes, *Biotechnol. Prog.* 20 (2004) 750–755. <https://doi.org/10.1021/bp0300568>.
- [86] F. Li, T. Chen, S. Hu, J. Lin, R. Hu, H. Feng, Superoxide Mediates Direct Current

- Electric Field-Induced Directional Migration of Glioma Cells through the Activation of AKT and ERK, *PLoS One*. 8 (2013). <https://doi.org/10.1371/journal.pone.0061195>.
- [87] K. Ziółkowska, R. Kwapiszewski, Z. Brzózka, Microfluidic devices as tools for mimicking the in vivo environment, *New J. Chem.* 35 (2011) 979–990. <https://doi.org/10.1039/c0nj00709a>.
- [88] S. Suresh, Biomechanics and biophysics of cancer cells, *Acta Biomater.* 3 (2007) 413–438. <https://doi.org/10.1016/j.actbio.2007.04.002>.
- [89] S.E.S.B.-O. F.Doljanski, Electro-kinetic properties of cells in growth processes: I. The electrophoretic behavior of liver cells during regeneration and post-natal growth, *Exp. Cell Res.* 26 (1962) 451–461.
- [90] F. Liebes, E. Pelle, *sec*, 57 (1981) 250–255.
- [91] J. Bauer, K. Hannig, Changes of the electrophoretic mobility of human monocytes are regulated by lymphocytes, *Electrophoresis.* 5 (1984) 269–274. <https://doi.org/10.1002/elps.1150050504>.
- [92] H.A. Pohl, K. Pollock, J.S. Crane, Dielectrophoretic force: A comparison of theory and experiment, *J. Biol. Phys.* 6 (1978) 133–160. <https://doi.org/10.1007/BF02328936>.
- [93] T. Kotnik, F. Bobanovid, <Sensitivity of transmembrane voltage induce PEF 1996.pdf>, 43 (1997) 285–291.
- [94] P.R.C. Gascoyne, S. Shim, Isolation of circulating tumor cells by dielectrophoresis, *Cancers (Basel)*. 6 (2014) 545–579. <https://doi.org/10.3390/cancers6010545>.
- [95] T.B. Jones, M. Washizu, Multipolar dielectrophoretic and electrorotation theory, *J. Electrostat.* 37 (1996) 121–134. [https://doi.org/10.1016/0304-3886\(96\)00006-X](https://doi.org/10.1016/0304-3886(96)00006-X).
- [96] S.A. Faraghat, K.F. Hoettges, M.K. Steinbach, D.R. Van Der Veen, W.J. Brackenbury, E.A. Henslee, F.H. Labeed, M.P. Hughes, High-Throughput, low-loss, low-cost, and label-free cell separation using electrophysiology-Activated cell enrichment, *Proc. Natl. Acad. Sci. U. S. A.* 114 (2017) 4591–4596. <https://doi.org/10.1073/pnas.1700773114>.
- [97] J. Yang, Y. Huang, X. Wang, X.B. Wang, F.F. Becker, P.R.C. Gascoyne, Dielectric properties of human leukocyte subpopulations determined by electrorotation as a cell separation criterion, *Biophys. J.* 76 (1999) 3307–3314. [https://doi.org/10.1016/S0006-3495\(99\)77483-7](https://doi.org/10.1016/S0006-3495(99)77483-7).
- [98] M. Elitas, E. Sengul, Quantifying Heterogeneity According to Deformation of the U937 Monocytes and U937-Differentiated Macrophages Using 3D Carbon Dielectrophoresis in Microfluidics, *Micromachines.* 11 (2020) 576. <https://doi.org/10.3390/mi11060576>.
- [99] R. Martinez-Duarte, F. Camacho-Alanis, P. Renaud, A. Ros, Dielectrophoresis of lambda-DNA using 3D carbon electrodes, *Electrophoresis.* 34 (2013) 1113–1122. <https://doi.org/10.1002/elps.201200447>.
- [100] Y. Yildizhan, U.B. Gogebakan, A. Altay, M. Islam, R. Martinez-Duarte, M. Elitas, Quantitative Investigation for the Dielectrophoretic Effect of Fluorescent Dyes at Single-Cell Resolution, *ACS Omega.* 3 (2018) 7243–7246. <https://doi.org/10.1021/acsomega.8b00541>.
- [101] Y. Yildizhan, N. Erdem, M. Islam, R. Martinez-Duarte, M. Elitas, Dielectrophoretic separation of live and dead monocytes using 3D carbon-electrodes, *Sensors (Switzerland)*. 17 (2017) 1–13. <https://doi.org/10.3390/s17112691>.
- [102] M. Elitas, Y. Yildizhan, M. Islam, R. Martinez-Duarte, D. Ozkazanc,

- Dielectrophoretic characterization and separation of monocytes and macrophages using 3D carbon-electrodes, *Electrophoresis*. 40 (2019) 315–321. <https://doi.org/10.1002/elps.201800324>.
- [103] E. Sengul, O. Kara, Y. Yildizhan, R. Martinez-Duarte, M. Elitas, Single Cell Level Dielectrophoretic Responses Dielectrophoretic Deformations of Monocytes to Quantify Population Heterogeneity, in: *Proc. Annu. Int. Conf. IEEE Eng. Med. Biol. Soc. EMBS, Institute of Electrical and Electronics Engineers Inc.*, 2020: pp. 2221–2226. <https://doi.org/10.1109/EMBC44109.2020.9176521>.
- [104] E. Sengul, M. Elitas, Single-Cell Mechanophenotyping in Microfluidics to Evaluate Behavior of U87 Glioma Cells, *Micromachines*. 11 (2020) 845. <https://doi.org/10.3390/mi11090845>.
- [105] M. Urbanska, M. Winzi, K. Neumann, S. Abuhattum, P. Rosendahl, P. Müller, A. Taubenberger, K. Anastassiadis, J. Guck, Single-cell mechanical phenotype is an intrinsic marker of reprogramming and differentiation along the mouse neural lineage, *Dev.* 144 (2017) 4313–4321. <https://doi.org/10.1242/dev.155218>.
- [106] F.J. Armistead, J. Gala De Pablo, H. Gadêlha, S.A. Peyman, S.D. Evans, Cells Under Stress: An Inertial-Shear Microfluidic Determination of Cell Behavior, *Biophys. J.* 116 (2019) 1127–1135. <https://doi.org/10.1016/j.bpj.2019.01.034>.
- [107] M.L. Pinto, E. Rios, C. Durães, R. Ribeiro, J.C. Machado, A. Mantovani, M.A. Barbosa, F. Carneiro, M.J. Oliveira, The two faces of tumor-associated macrophages and their clinical significance in colorectal cancer, *Front. Immunol.* 10 (2019) 1–12. <https://doi.org/10.3389/fimmu.2019.01875>.
- [108] I. Müller, D. Kulms, A 3D organotypic melanoma spheroid skin model, *J. Vis. Exp.* 2018 (2018) 1–9. <https://doi.org/10.3791/57500>.
- [109] A.B. Theberge, J. Yu, E.W.K. Young, W.A. Ricke, W. Bushman, D.J. Beebe, Microfluidic Multiculture Assay to Analyze Biomolecular Signaling in Angiogenesis, *Anal. Chem.* 87 (2015) 3239–3246. <https://doi.org/10.1021/ac503700f>.
- [110] T.H. Hsu, Y.L. Kao, W.L. Lin, J.L. Xiao, P.L. Kuo, C.W. Wu, W.Y. Liao, C.H. Lee, The migration speed of cancer cells influenced by macrophages and myofibroblasts co-cultured in a microfluidic chip, *Integr. Biol.* 4 (2012) 177–182. <https://doi.org/10.1039/c2ib00112h>.
- [111] D. Campos, V. Méndez, I. Llopis, Persistent random motion: Uncovering cell migration dynamics, *J. Theor. Biol.* 267 (2010) 526–534. <https://doi.org/10.1016/j.jtbi.2010.09.022>.
- [112] I.D. Luzhansky, A.D. Schwartz, J.D. Cohen, J.P. MacMunn, L.E. Barney, L.E. Jansen, S.R. Peyton, Anomalous diffusing and persistently migrating cells in 2D and 3D culture environments, *APL Bioeng.* 2 (2018) 026112. <https://doi.org/10.1063/1.5019196>.
- [113] Y. Choi, E. Hyun, J. Seo, C. Blundell, H.C. Kim, E. Lee, S.H. Lee, A. Moon, W.K. Moon, D. Huh, A microengineered pathophysiological model of early-stage breast cancer, *Lab Chip*. 15 (2015) 3350–3357. <https://doi.org/10.1039/c5lc00514k>.
- [114] A.L. Paguirigan, D.J. Beebe, Microfluidics meet cell biology: Bridging the gap by validation and application of microscale techniques for cell biological assays, *BioEssays*. 30 (2008) 811–821. <https://doi.org/10.1002/bies.20804>.
- [115] S. Jain, S. Swain, L. Das, S. Swain, L. Giri, A.K. Kondapi, H.N. Unni, Microfluidic protein imaging platform: Study of tau protein aggregation and alzheimer’s drug response, *Bioengineering*. 7 (2020) 1–13.

- <https://doi.org/10.3390/bioengineering7040162>.
- [116] L. Zhu, X.L. Peh, H.M. Ji, C.Y. Teo, H.H. Feng, W.T. Liu, Cell loss in integrated microfluidic device, *Biomed. Microdevices.* 9 (2007) 745–750. <https://doi.org/10.1007/s10544-007-9085-z>.
- [117] A. Fayzullin, C.J. Sandberg, M. Spreadbury, B.M. Saberniak, Z. Grieg, E. Skaga, I.A. Langmoen, E.O. Vik-Mo, Phenotypic and Expressional Heterogeneity in the Invasive Glioma Cells, *Transl. Oncol.* 12 (2019) 122–133. <https://doi.org/10.1016/j.tranon.2018.09.014>.
- [118] J.J. Parker, P. Canoll, L. Niswander, B.K. Kleinschmidt-DeMasters, K. Foshay, A. Waziri, Intratumoral heterogeneity of endogenous tumor cell invasive behavior in human glioblastoma, *Sci. Rep.* 8 (2018) 1–10. <https://doi.org/10.1038/s41598-018-36280-9>.
- [119] K. Kolli-Bouhafs, A. Boukhari, A. Abusnina, E. Velot, J.P. Gies, C. Lugnier, P. Rondé, Thymoquinone reduces migration and invasion of human glioblastoma cells associated with FAK, MMP-2 and MMP-9 down-regulation, *Invest. New Drugs.* 30 (2012) 2121–2131. <https://doi.org/10.1007/s10637-011-9777-3>.
- [120] S. Sheykhzadeh, M. Luo, B. Peng, J. White, Y. Abdalla, T. Tang, E. Mäkilä, N.H. Voelcker, W.Y. Tong, Transferrin-targeted porous silicon nanoparticles reduce glioblastoma cell migration across tight extracellular space, *Sci. Rep.* 10 (2020) 1–17. <https://doi.org/10.1038/s41598-020-59146-5>.
- [121] P. Monzo, Y.K. Chong, C. Guetta-Terrier, A. Krishnasamy, S.R. Sathe, E.K.F. Yim, W.H. Ng, B.T. Ang, C. Tang, B. Ladoux, N.C. Gauthier, M.P. Sheetz, Mechanical confinement triggers glioma linear migration dependent on formin FHOD3, *Mol. Biol. Cell.* 27 (2016) 1246–1261. <https://doi.org/10.1091/mbc.E15-08-0565>.
- [122] L. Prah, M. Stanslaski, P. Vargas, M. Piel, D. Odde, Glioma cell migration in confined microchannels via a motor-clutch mechanism, (2018) 1–30. <https://doi.org/10.1101/500843>.
- [123] J. Sabari, D. Lax, D. Connors, I. Brotman, E. Mindrebo, C. Butler, I. Entersz, D. Jia, R.A. Foty, Fibronectin matrix assembly suppresses dispersal of glioblastoma cells, *PLoS One.* 6 (2011). <https://doi.org/10.1371/journal.pone.0024810>.
- [124] A. Kiss, P. Horvath, A. Rothballer, U. Kutay, G. Csucs, Nuclear motility in glioma cells reveals a cell-line dependent role of various cytoskeletal components, *PLoS One.* 9 (2014). <https://doi.org/10.1371/journal.pone.0093431>.
- [125] J. Dou, S. Mao, H. Li, J.M. Lin, Combination Stiffness Gradient with Chemical Stimulation Directs Glioma Cell Migration on a Microfluidic Chip, *Anal. Chem.* 92 (2020) 892–898. <https://doi.org/10.1021/acs.analchem.9b03681>.
- [126] D. Irimia, M. Toner, Spontaneous migration of cancer cells under conditions of mechanical confinement, *Integr. Biol.* 1 (2009) 506–512. <https://doi.org/10.1039/b908595e>.
- [127] T.W. Remmerbach, F. Wottawah, J. Dietrich, B. Lincoln, C. Wittekind, J. Guck, Oral cancer diagnosis by mechanical phenotyping, *Cancer Res.* 69 (2009) 1728–1732. <https://doi.org/10.1158/0008-5472.CAN-08-4073>.
- [128] J. Banyard, D.R. Bielenberg, The role of EMT and MET in cancer dissemination, *Connect. Tissue Res.* 56 (2015) 403–413. <https://doi.org/10.3109/03008207.2015.1060970>.
- [129] J. Bai, G. Adriani, T.M. Dang, T.Y. Tu, H.X.L. Penny, S.C. Wong, R.D.R.D. Kamm, J.P. Thiery, Contact-dependent carcinoma aggregate dispersion by M2a macrophages

- via ICAM-1 and $\beta 2$ integrin interactions, *Oncotarget*. 6 (2015) 25295–25307. <https://doi.org/10.18632/oncotarget.4716>.
- [130] T. Shibue, R.A. Weinberg, EMT, CSCs, and drug resistance: The mechanistic link and clinical implications, *Nat. Rev. Clin. Oncol.* 14 (2017) 611–629. <https://doi.org/10.1038/nrclinonc.2017.44>.
- [131] A. Grigore, M. Jolly, D. Jia, M. Farach-Carson, H. Levine, Tumor Budding: The Name is EMT. Partial EMT., *J. Clin. Med.* 5 (2016) 51. <https://doi.org/10.3390/jcm5050051>.
- [132] D. Hanahan, R.A. Weinberg, Hallmarks of cancer: The next generation, *Cell*. 144 (2011) 646–674. <https://doi.org/10.1016/j.cell.2011.02.013>.